A Climatology of Waves in the Equatorial Region

PAUL E. ROUNDY AND WILLIAM M. FRANK

Department of Meteorology, The Pennsylvania State University, University Park, Pennsylvania

(Manuscript received 26 March 2003, in final form 12 March 2004)

ABSTRACT

Propagating anomalies of moisture and moist deep convection in the Tropics are organized into a variety of large-scale modes. These include (but are not limited to) the so-called intraseasonal oscillations, convectively coupled waves similar to those predicted by shallow water theory on the equatorial beta plane, and tropical-depression-type disturbances. Along with the annual and diurnal cycles, these modes act and interact to control much of the variance of tropical convection. Analyses of 10 yr of outgoing longwave radiation (OLR) and precipitable water (PW) data are carried out to develop comparative climatologies of these wavelike modes. The analysis relaxes the commonly used cross-equatorial symmetry constraints, which allows study of the portions of the wavelike processes that are asymmetric across the equator.

Mean background states are found for OLR and for PW as functions of day of the year. Examination of anomalies together with the background reveals much about how the waves are affected by their environments. Zonal wavenumber–frequency spectral analyses are performed on these anomalies. Following the spectral analyses, the OLR and the PW data are then filtered for specific regions of the wavenumber–frequency domain. Results show how variance generated by propagating modes is distributed in time and space, approximately illustrating the relative contributions of the wave modes to regional OLR and PW variability.

1. Introduction

This work presents a climatology of synoptic- and planetary-scale propagating modes in the Tropics. As we will discuss later, many others have done similar work from a more theoretical perspective. This paper focuses on five different propagating modes and their effects on tropical cloudiness and humidity. This is a first step toward the ultimate goal of determining where, when, and how much these waves directly affect tropical weather.

Theoretical and observational studies of the tropical atmosphere have led to detailed analyses of wavelike disturbances that propagate generally parallel to the equator. Most of these disturbances (hereafter often called ''waves'' for simplicity) are triggered either by diabatic heating associated with organized deep convection, by interaction of other disturbances with land (e.g., Kleeman 1989), or by forcing from midlatitudes (e.g., Straub and Kiladis 2003a). These waves modulate tropical convection and rainfall and may frequently affect midlatitude weather by influencing tropical cyclogenesis (e.g., Dickinson and Molinari 2002) or by inducing teleconnections.

The basic structures of many of these tropical waves are predicted by linear equatorial beta-plane shallow-water theory (Matsuno 1966; Lindzen 1967), but shallow water theory alone is insufficient to explain much of the behavior observed in the atmosphere. Wave structure and dispersion characteristics such as amplitude, wavenumber, and frequency may be modified by nonlinear interactions between the waves (e.g., Straub and Kiladis 2003b), by interactions with base-state winds (Zhang and Geller 1994; Zhang and Webster 1989; Wheeler and Kiladis 1999, hereafter WK99), and by moist convection (Chang and Piwowar 1974; Lindzen 1974; Kuo 1975; and others) modulated by the background base state including sea surface temperature (SST; Hess et al. 1993) to produce the observed behavior.

Observations do suggest the existence of atmospheric modes that are similar to several of the theoretically predicted waves, such as mixed Rossby–gravity (MRG), inertio–gravity [IG, westward propagating (WIG), eastward propagating (EIG)], Kelvin, and equatorial Rossby (ER). The theoretical forms of these waves are characterized by meridional mode number n and equivalent depth (a parameter that determines meridional width of anomalies and wave frequency at a given wavenumber). Other propagating modes are observed, but are perhaps not clearly predicted by the linear theory [e.g., the intraseasonal or Madden–Julian oscillations (ISO or MJO; Madden and Julian 1994) and tropical-depression-type disturbances (TD-type disturbances; Liebmann and

Corresponding author address: Paul Roundy, CIRES, University of Colorado, NOAA/Aeronomy Laboratory, 325 Broadway, Boulder, CO 80305-3328.
E-mail: proundy@al.noaa.gov

Hendon 1990; Takayabu and Nitta 1993; Takayabu 1994; WK99)].

Low meridional modes of convectively coupled equatorial waves have been detected from outgoing longwave radiation (OLR) data collected from near-polar orbiting satellites (Dunkerton and Crum 1995; Takayabu 1994; WK99; and others). These waves are referred to as being convectively coupled because moist deep convection is associated with them. The release of latent heat associated with this convection apparently affects wave structure and propagation statistics. WK99 noted that coupled waves propagate more slowly than their uncoupled counterparts, and thus are characterized by smaller equivalent-depth parameters. OLR is often used to track convectively coupled waves because it is a relatively good tracer of deep tropical convection. Other studies have used dynamical fields and station observations to identify the waves (e.g., Pires et al. 1997; Liebmann and Hendon 1990).

WK99 produced a thorough analysis of convectively coupled waves in the equatorial region. They examined portions of the waves that are symmetric or antisymmetric across the equator by applying the symmetric and antisymmetric filters to their data (e.g., Yanai and Murakami 1970). They revealed that many of the observed waves are similar to those expected from shallow water theory. We extend their analysis technique by relaxing the symmetry constraints such that the asymmetric portions of the waves can be examined in the context of the background state.

We further extend the analysis by utilizing precipitable water (PW) data together with OLR. Precipitable water responds more rapidly at large scales than does OLR to low-level vertical forcing, as shown below. It also exhibits greater sensitivity to horizontal advection than OLR does. The more rapid response of PW is a result of the higher concentration of water vapor near the surface than aloft. Precipitable water appears to trace waves better than OLR does through regions in which large-scale convection is suppressed by the base state. Hence, PW is useful for tracking waves as they pass from regions of enhanced convection to regions of suppressed convection, and vice versa. Variations in PW data are approximately of the same order of magnitude in clear and in convectively disturbed areas. We show later that, unlike OLR, PW tends to vary most at the edges of active convective regions rather than at their centers—evidence that PW is more sensitive than OLR to horizontal advection. Precipitable water anomalies are often somewhat out of phase with OLR anomalies because PW does not tend to continue to increase in proportion to increases in vertical velocity and rainfall throughout the life cycle of a large-scale convective system.

2. Methods

a. Data

Most of our OLR and PW data were derived from radiation measurements collected from near-polar orbiting satellites following nearly sun-synchronous orbits. The PW and the OLR data were analyzed and filtered in similar ways, as discussed below.

1) PRECIPITABLE WATER

The National Aeronautics and Space Administration (NASA) Water Vapor Project (NVAP) provided daily PW data. NVAP total column PW is given in millimeters on a 1° grid for the period 1 January 1988 through 31 December 1997. A description of this dataset and its derivation are given by Randel et al. (1996).

The NVAP data were arranged into longitude–time arrays, including one for each latitude from 20°N to 20°S. Small sections of missing data were filled by simple temporal linear interpolation.

2) OLR

Daily OLR data on a 2.5° grid for 1 January 1988 through 31 December 1997 were acquired from the National Oceanic and Atmospheric Administration (NOAA) near-polar-orbiting satellites and the National Environmental Satellite Data and Information Service (NESDIS). Missing data points were estimated by using spatial and temporal interpolation (Liebmann and Smith 1996). The date range was limited to make it identical to that of the PW.

b. Base state

The annual cycle was subtracted from each OLR and PW grid point time series. The cycle was found by calculating the mean value over the 10 yr for each day of the year and smoothing the result with a 43-day centered moving average. The 43-day smoothing was sufficient to remove most high-frequency signals remaining after the 10-yr average was calculated. This cycle represents an estimate of the mean base state over which the anomalies in the rest of the analyses propagate.

c. Spectra

This study employs zonal space–time spectral analysis and filtering of OLR and PW data in the wavenumber–frequency domain to study waves that are dominated by zonal propagation. The spectral analysis finds the distribution of power in the wavenumber–frequency domain associated with the propagating modes. The filtering approximates the longitude–time behavior that is associated with specific regions of the wavenumber–frequency domain. Pires et al. (1997), Takayabu (1994), WK99, and Straub and Kiladis (2002) performed similar spectral analysis and filtering.

Space–time spectral analyses were performed on the OLR and the PW anomaly grids in a manner similar to that used by WK99. This analysis was performed as discussed in the appendix.

Raw spectra were calculated in four formats. These were for data that were symmetric or antisymmetric across the equator and for data from only the Northern or Southern Hemispheres. The Northern Hemisphere spectrum is the mean spectral estimate for all longitude–time arrays that represent latitudes from 1° to 15°N latitude, and similarly, the Southern Hemisphere spectrum is limited to 1° to 15°S latitude. The longitude–time series used to calculate the symmetric and the antisymmetric spectra were developed by using the symmetric and antisymmetric filters, as done by WK99.

d. Filtering

After performing the spectral analyses, regions of the spectrum were isolated in the wavenumber–frequency domains of both variables and applied as Fourier filters, as done by WK99, except that we did not apply symmetry filtering. Straub and Kiladis (2002) filtered OLR data in the wavenumber–frequency domain to isolate the time–longitude behavior of disturbances that are associated with the atmospheric counterparts of the equatorial Kelvin mode. They studied convective anomalies produced by these Kelvin waves in the eastern tropical Pacific basin without applying symmetry filters. This allowed them to view asymmetries in filtered OLR that are attributable to the effect of the base-state SSTs on moist deep convection, which, instead of being centered on the equator, like the divergence pattern of a theoretical Kelvin wave, they were centered near the convective maximum of the intertropical convergence zone (ITCZ) between 2° and 7°N. We follow their lead in examining other wave types.

WK99 identified regions in the OLR wavenumber–frequency domain that are assumed to be dominated by the signals of specific theoretical convectively coupled equatorial waves over a narrow range of equivalent depths. We selected similar regions (as in Fig. 6 of WK99, with some modifications) and we added another region representative of TD-type disturbances.

e. Computing climatologies

Variance climatologies of the filtered data were developed to reveal when wavelike activity tends to occur and where it is locally most active. Seasonal variance maps of filtered and unfiltered OLR and PW anomalies (similar to those of WK99) were obtained by placing 91-day segments of time series (for each grid point) into appropriate seasonal bins, appending data from each season of each year to data from the same season of the previous year, and finding the time variance of the result. Relative maxima in these variance maps are analogous to the mean tracks of anomalies in the filtered data. This was done for both unfiltered and filtered OLR and PW anomalies. We then found the global mean annual cycle of variance of each filtered dataset. This was done by averaging the squares of the global PW and OLR anomalies in space, then averaging the result according to day of the year.

3. Results

a. Base-state annual cycle maps

Figure 1 shows the mean values of the OLR and PW from the smoothed annual cycle for 21 December, 21 March, 21 June, and 21 September. These maps are examples of the base PW and OLR states over which anomalies in the rest of the analyses propagate on the given dates in the typical year.

The mean background patterns are rarely precisely symmetric about the equator. Therefore, the climatological regions of base-state modulated convective feedbacks are more likely to be asymmetric across the equator than they are to be purely antisymmetric or symmetric.

The most obvious features of the maps in Fig. 1 are the signatures of the intertropical convergence zones, the South Pacific convergence zone, and the differences between land and sea. The darkest shaded regions that form zonal bands represent the mean OLR and PW signatures of the convergence zones. Land also influences the background OLR and PW. Precipitable water is generally reduced above land, especially above higher terrain, which replaces the vapor-rich layers of the lower atmosphere. In contrast, OLR measured over land may be higher or lower than over the surrounding ocean because topography or surface temperature variations may enhance or suppress local deep convection.

The meridional behavior of PW is different from and somewhat simpler than that of OLR. Between 20°N and 20°S, PW decays away from the convergence zones toward the Poles, but OLR is minimum near the convergence zones, increases toward the centers of subtropical high-pressure regions, and then decreases again toward the midlatitudes (e.g., Figs. 1e and 1g over the South Pacific and South Atlantic basins, there is a local OLR maximum, south of which, OLR decreases poleward).

b. Spectra

The spectral analyses reveal the distribution of power in the wavenumber–frequency domain of synoptic- and planetary-scale modes. The OLR background (not shown) is similar to that of WK99. The raw PW spectrum (not shown) is smoother than the raw OLR spectrum, and its power is shifted more toward westward propagation. The normalized spectra for OLR and for PW are presented in Figs. 2 and 3, respectively. Shading in Figs. 3 and 4 begins near the level of 90% significance above the background, as estimated by a bootstrap-resampling test (see appendix and Wilks 1995).

Among the most obvious differences between the OLR and the PW spectra is that the peaks in the PW spectrum are not as distinct as those in the OLR spec-

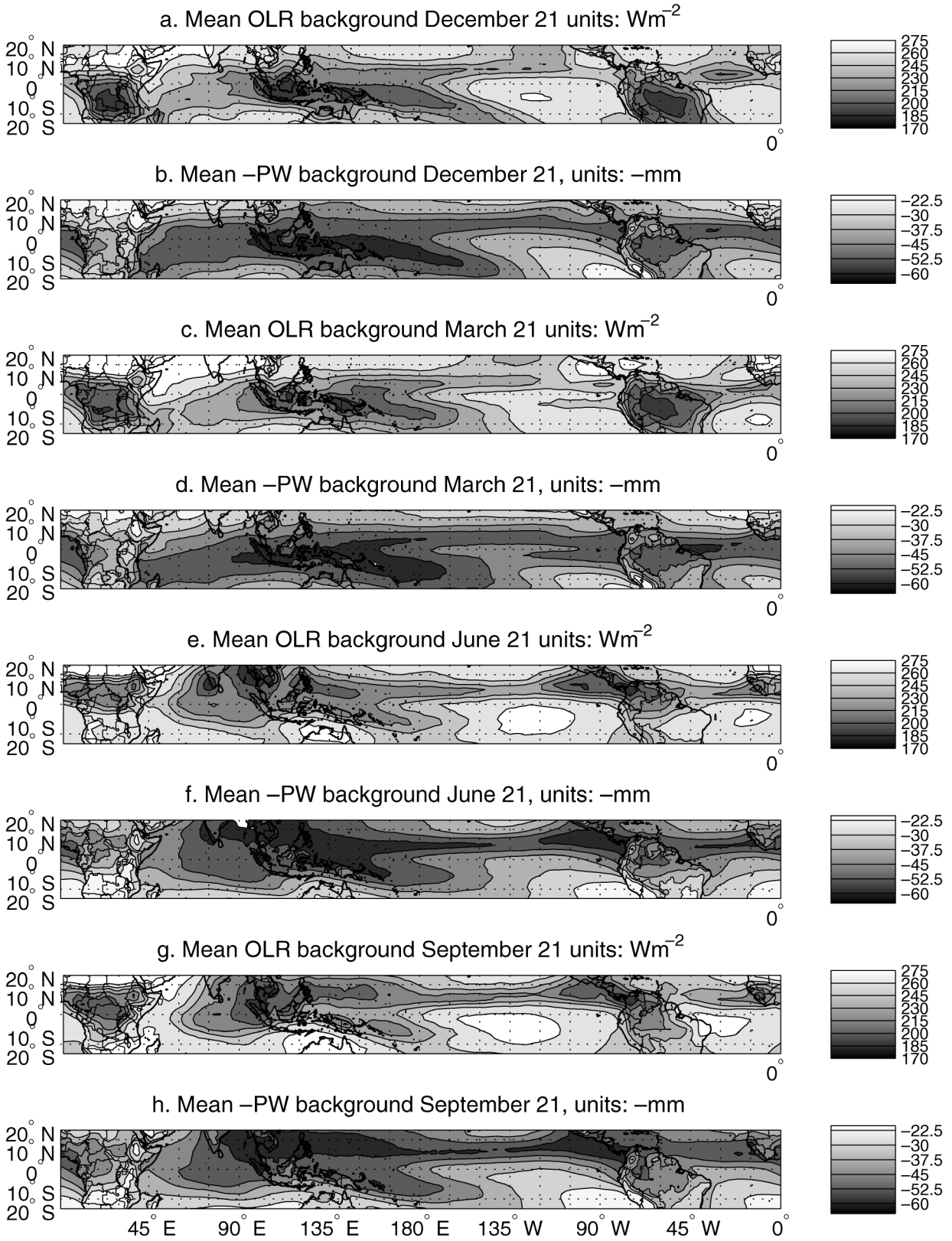

FIG. 1. Approximate mean backgrounds of OLR and PW indicating the distribution of these quantities according to day of year. (a), (b) The backgrounds for 21 Dec of OLR and PW, respectively. (c), (d) The OLR and PW results for 21 Mar. (e), (f) The results for 21 Jun. (g), (h) The results for 21 Sep.

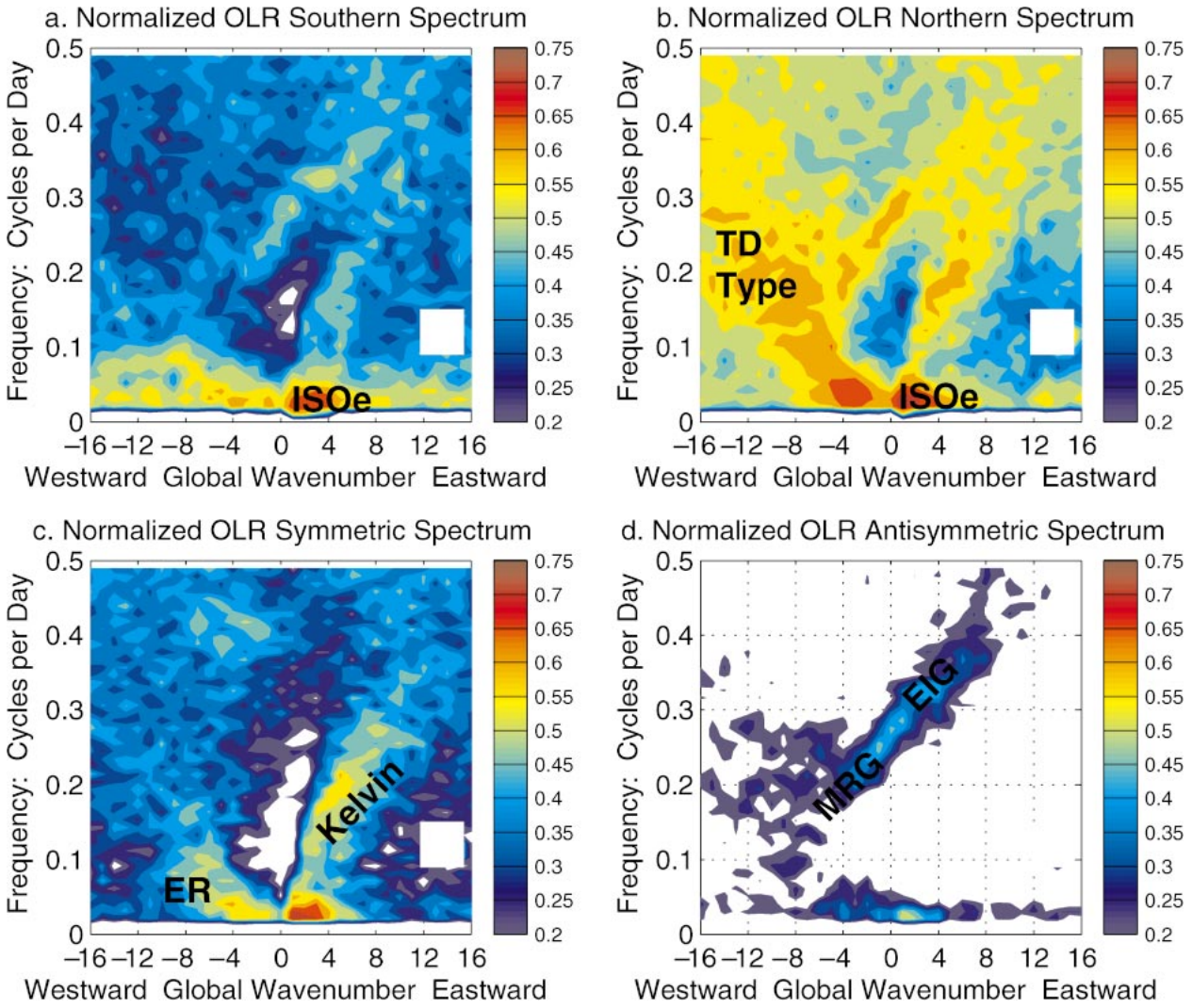

FIG. 2. Normalized OLR spectra. (a), (b) The estimates for the Southern and Northern Hemispheres, respectively. (c), (d) The estimates for data that have been filtered for symmetric and antisymmetric cross-equatorial symmetries, respectively. Peaks associated with dominant modes are labeled. White rectangles hide a peak that is generated by aliasing from the satellite swath path size and frequency (see WK99). Shading begins near the 90% level of significance above the background.

trum. Some peaks, especially those of antisymmetric modes, are only marginally significant above the background. However, the analysis below reveals that the PW data resolve a greater range of disturbances than do the OLR data. The apparent lack of normalized PW power in most bands is actually due to this greater sensitivity to weaker or less convectively coupled waves that are not as apparent in the OLR data. These additional waves broaden the peaks in the raw PW spectrum, such that the peaks of the convectively coupled waves stand out less clearly against the background. In fact, such broad peaks contribute to the background itself because the smoothing may not completely remove them. Thus, the apparent lack of normalized power in the bands of convectively coupled waves does not mean that PW is insensitive to most of these waves, but rather it is sensitive to a broader range of them.

We provide information about cross-equatorial asymmetries by comparing the Northern Hemisphere spectrum with the Southern Hemisphere spectrum. The principal propagating modes are labeled near the peaks that are probably dominated by their signals.

The hemispheric spectra (Figs. 2a,b and 3a,b) reveal that all modes, including those similar to theoretical beta-plane modes (labeled in Figs. 2c,d and 3c,d) exhibit cross-equatorial asymmetry because the distribution of power differs between the hemispheres.

Most regions of the Northern Hemisphere spectrum contain more power than the same regions of the Southern Hemisphere spectrum. The major exception is the

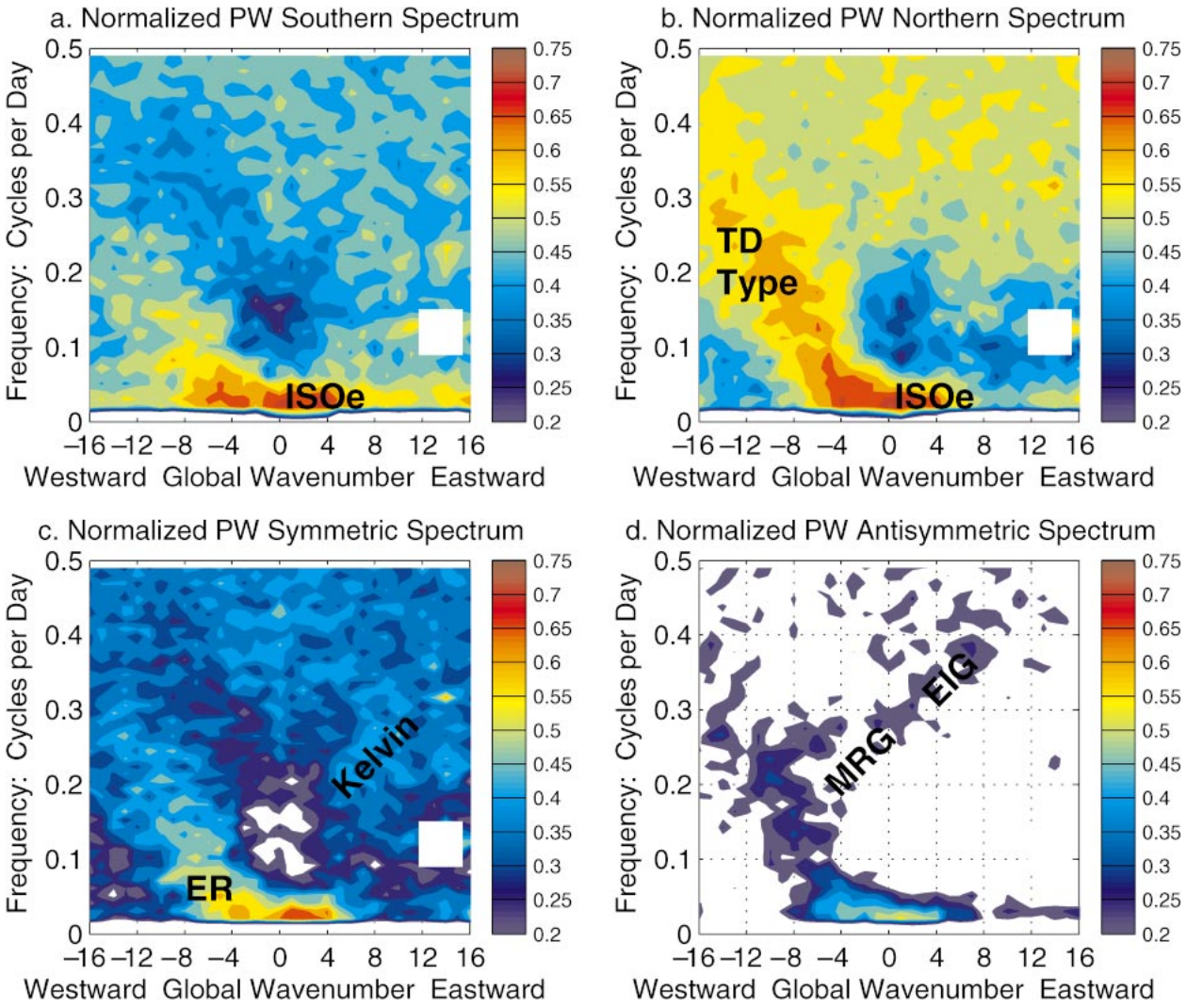

FIG. 3. Same as Fig. 2, except for PW.

ISOe, which is strongest in the Southern Hemisphere. Analysis indicates that the hemispheric asymmetry of the ISOe is strongly related to its seasonality. During the northern and southern summer months, the ISOe tends to be highly asymmetric. It appears most symmetric when averaged over the entire year (see also Hendon and Salby 1994), but our results (and those of WK99) show that it also contributes to the antisymmetric spectrum.

The Kelvin mode (which is symmetric across the equator in the linear theory) also exhibits asymmetry in the spectrum. Though the Kelvin wave signal has a strong symmetric component across the equator in these data (Fig. 2c), there is marked Northern Hemisphere dominance (Figs. 2a,b), which we explain later in section 3c(5).

The mostly asymmetric TD-type disturbances dominate the 3–10-day westward wavenumber 8–16 portion of the spectra (WK99), especially in the Northern Hemisphere. A broad region of significant power joins the regions dominated by ER-, MRG-, and TD-type disturbances in the Northern Hemisphere in both the OLR and the PW results. There is little distinction between the peaks associated with these wave types, consistent with the idea that a wave of one meridional structure may evolve into a wave of another by refractive or convective feedback processes without major alteration of its phase propagation statistics. Takayabu and Nitta (1993) and Dickinson and Molinari (2002) have found that MRG-like waves may migrate off the equator to evolve into TD-type disturbances. The overlapping portions of peaks imply that any filter designed to isolate one specific wave type may contain other wave types as well.

The dominance of one hemisphere over the other implies that asymmetric portions of anomaly patterns are a significant component of the global OLR and PW spectra. It is important to note that symmetric and an-

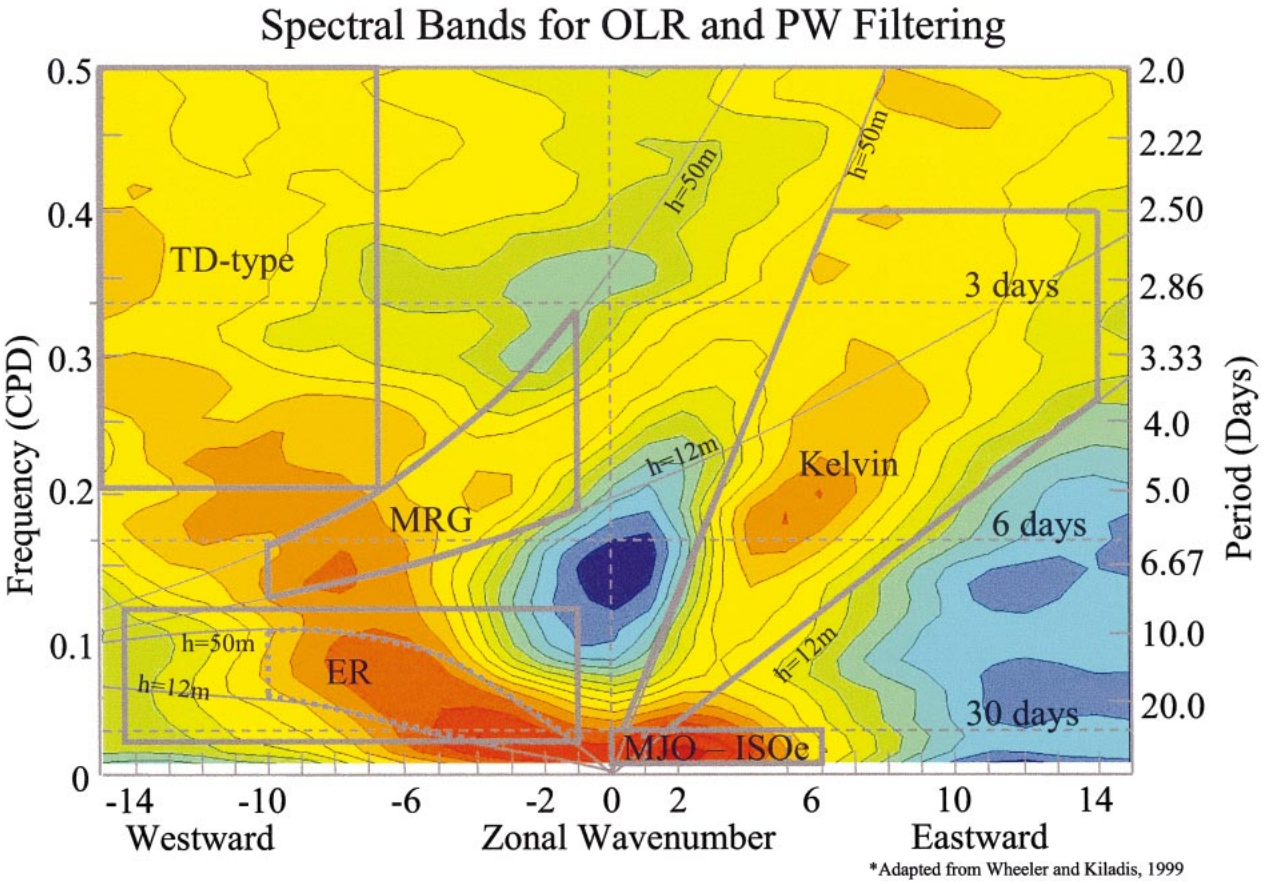

FIG. 4. Spectral bands of the five filters used in the project are outlined with solid curves and plotted over a smoothed tropical OLR spectrum. Where these filters differ from those of WK99, their corresponding filters are enclosed by dotted lines.

tisymmetric filtered data share the signal of such asymmetric waves equally. Therefore, a substantial portion of the spectra obtained using symmetric and antisymmetric filters is produced by the actions of the filters being applied to anomaly patterns that exhibit cross-equatorial asymmetries.

Figures 2c,d and 3c,d represent the PW and OLR spectra of symmetric and antisymmetric filtered data, respectively, comparable with Fig. 3 of WK99. Our OLR spectra are almost identical to those of WK99, except that ours indicate more significant power in the regions of TD-type disturbances and in the region of low-frequency westward propagation, and somewhat less significant power in the MRG–EIG band.

In summary, comparison of all parts of the symmetry-specific spectra with the hemispheric spectra reveals that our symmetry spectra and those of WK99 contain large amounts of power contributed by asymmetric cross-equatorial patterns.

c. Filtering results

1) OVERVIEW

Filter bands included in this study (shown plotted over the tropical mean OLR spectrum in Fig. 4) are designed to capture the ISOe (the eastward-propagating portion of the ISO), TD-type disturbances, and Kelvin, ER, and MRG waves. Our filter bands for quasi-linear modes are labeled according to the dominant linear mode that is expected to occur in the box according to the results of WK99. The other two filters were named for the processes observed to dominate the band. Our ER filter is square, including wavenumbers 1–14 westward and periods of 9.7–48 days. The points contained in the ER $n = 1$ filter of WK99 are a subset of the points contained in our ER filter. Our ISOe and ER filters are larger than the corresponding filters of WK99 because we found that the expansions allowed them to better represent disturbances seen in unfiltered data. The TD-type filter includes wavenumbers 6–16 and periods of 2–5 days. This band was selected because it was consistent with observations of TD-type disturbances, and because we did not want it to overlap with the MRG filter. Our Kelvin and MRG filters were identical to those of WK99.

We selected for presentation here a portion of the filtered data climatology identical to that used by WK99, to facilitate comparison with their results. The time period chosen was 1 September 1992 through 1 April

1993. This discussion focuses on one filter band at a time, beginning with the ER band, then proceeding with the ISOe-, Kelvin-, MRG-, and TD-type bands. For each filter band we present a selected ''snapshot'' plan-view map of the filtered data, a Hovmoeller diagram, and maps of variance. The results for each filter band may be compared with the unfiltered anomalies and with their seasonal variance patterns, which are given in Figs. 5, and 6, respectively. Figure 7 gives the global annual cycles of variance for the unfiltered and filtered OLR and PW anomalies.

The horizontal snapshot of each type of filtered data is shown to simplify the discussion of horizontal anomaly patterns (e.g., Fig. 8). The specific dates for these snapshots were chosen because they gave particularly interesting patterns, not because of their level of conformity to linear theory. The snapshots include filtered European Centre for Medium-Range Forecasts (ECMWF) reanalysis winds (filtered in the same manner as the OLR and the PW). For reference, theoretical horizontal structures of the linear modes can be found in Matsuno (1996) and in Wheeler et al. (2000). The example Hovmoeller diagrams of the filtered data are centered on latitudes of consistently high activity in the band (e.g., Fig. 9). All Hovmoeller results for filtered data are normalized by the tropical global mean (20°N–20°S) anomaly absolute value so that OLR and PW results could be objectively compared.

2) Raw anomalies and total variance

Hovmoeller diagrams of the raw PW and OLR anomalies averaged from the equator to 7.5°N are given in Figs. 5a and 5b, respectively. Most of the anomalies in the filtered data discussed below also appear in the raw data. Note that the PW anomalies appear to trace the westward-propagating modes across the Pacific basin from 120°W to the date line more consistently than the OLR anomalies, particularly over the East Pacific.

Figure 6 gives the total seasonal variance of PW and OLR anomalies that is not associated with the annual or diurnal cycles. Comparison of these maps with Fig. 2 highlights the different behavior of OLR and PW. OLR appears to vary most where its mean value is lowest, where convection tends to be most active (Figs. 2c and 6c). As a result, OLR is a good wave tracer in convectively active regions. OLR varies least in the centers of the subtropical high pressure regions of the southeastern Pacific and southern Atlantic basins. In contrast, PW usually varies most where the horizontal gradients of mean PW are highest, indicating that horizontal advection of PW generates an important part of PW variance in those regions. For example, PW is highest near the equator, but it varies most more poleward from these active regions, where horizontal PW gradients are high (Figs. 2d, 6d). OLR exhibits enhanced variance over the oceans near monsoon regions during the seasons when those monsoons are active (e.g., southern Asia, northern Australia). Precipitable water also shows enhanced variance in those regions, but to a lesser extent over land.

Figures 7a and 7g show that the mean variance over the Tropics of PW is more or less constant through the year, whereas OLR appears to have maximum at the end of the Northern Hemisphere fall and another early in the northern spring. An apparent minimum appears during the Northern Hemisphere summer, presumably because of a simultaneous minimum of intraseasonal convection.

3) Equatorial Rossby wave band-filtered data

Figure 8 gives the ER-filtered OLR, PW, and 300-hPa winds for 4 January 1993. The mode-1 waves are severely distorted from their theoretical patterns. None of the anomalies associated with the waves in Fig. 8 appears to exhibit cross-equatorial symmetry, though the gyres do appear to be distorted forms of the $n = 1$ ER mode [e.g., Matsuno (1996) and many others].

Figure 9 gives an ER filter band longitude–time segment at 10°N, where OLR and PW variance in this band tends to be consistently active throughout the annual cycle. More waves appear in our Western Hemisphere OLR result than in the result of WK99 because of our larger filter band (the anomalies tend to be of smaller spatial scale there, so including higher wavenumbers is necessary to resolve them). Precipitable water appears to vary more consistently than OLR with waves in this spectral region.

Figure 10 is the set of variance maps for the OLR and the PW that is filtered for the ER wavenumber–frequency band. Precipitable water responds to waves in the ER band more than any other band; thus, ER anomalies dominate the total PW variance (Fig. 6). The ER spectral region appears to be dominated by waves of meridional mode $n = 1$, but the data may contain other modes, as discussed previously. The region of greatest variance in ER-filtered PW is in the Northern Hemisphere west of the date line during the Southern Hemisphere summer. Meridional gradients there are high, so horizontal advection probably plays a roll in producing this maximum. The greatest OLR variance occurs in the same region, except during the northern summer. Significant asymmetries are visible in the variance patterns of both data types, but throughout the annual cycle, most bands of high variance appear to have a corresponding variance track in the opposite hemisphere.

Figures 7b and 7h show the approximate annual cycles of variance for the ER band-filtered PW and OLR data, respectively. Both OLR and PW have brief periods of activity that appear to be slightly more enhanced than the annual mean, including a period between the southern summer and the northern spring, and another period during the northern fall, indicating

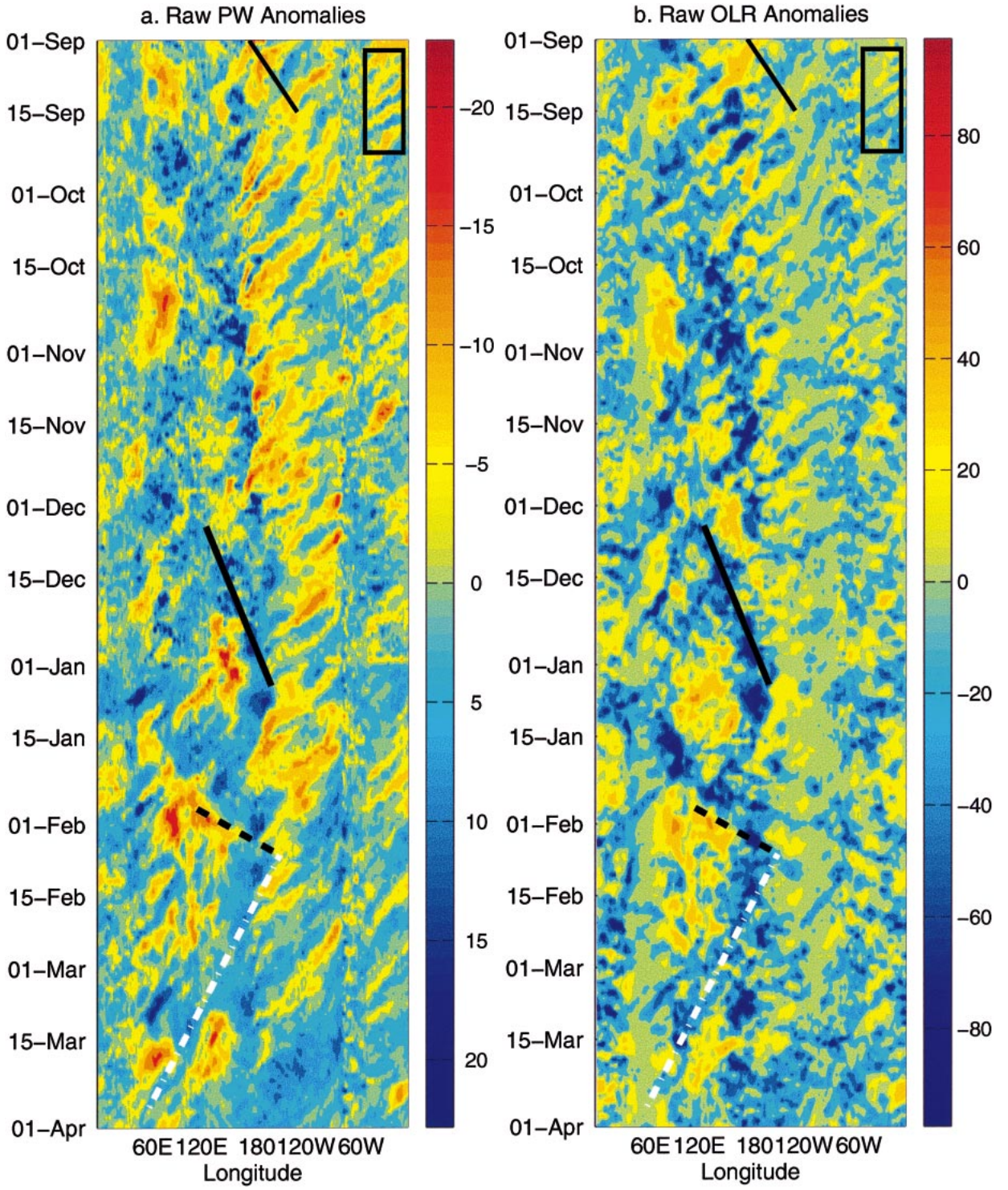

FIG. 5. Unfiltered anomalies of (a) PW and (b) OLR for 1 Sep 1992–1 Apr 1993. Data are averaged from the equator to 7.5°N. The shading schemes of the OLR and PW data were normalized by the zonal and time mean absolute values of the same OLR and PW datasets, so that amplitudes could be objectively compared. Lines and rectangles drawn on the diagram are included for the convenience of the reader, for comparison with the filtered data shown later in Figs. 9, 12, 15, 18, and 22.

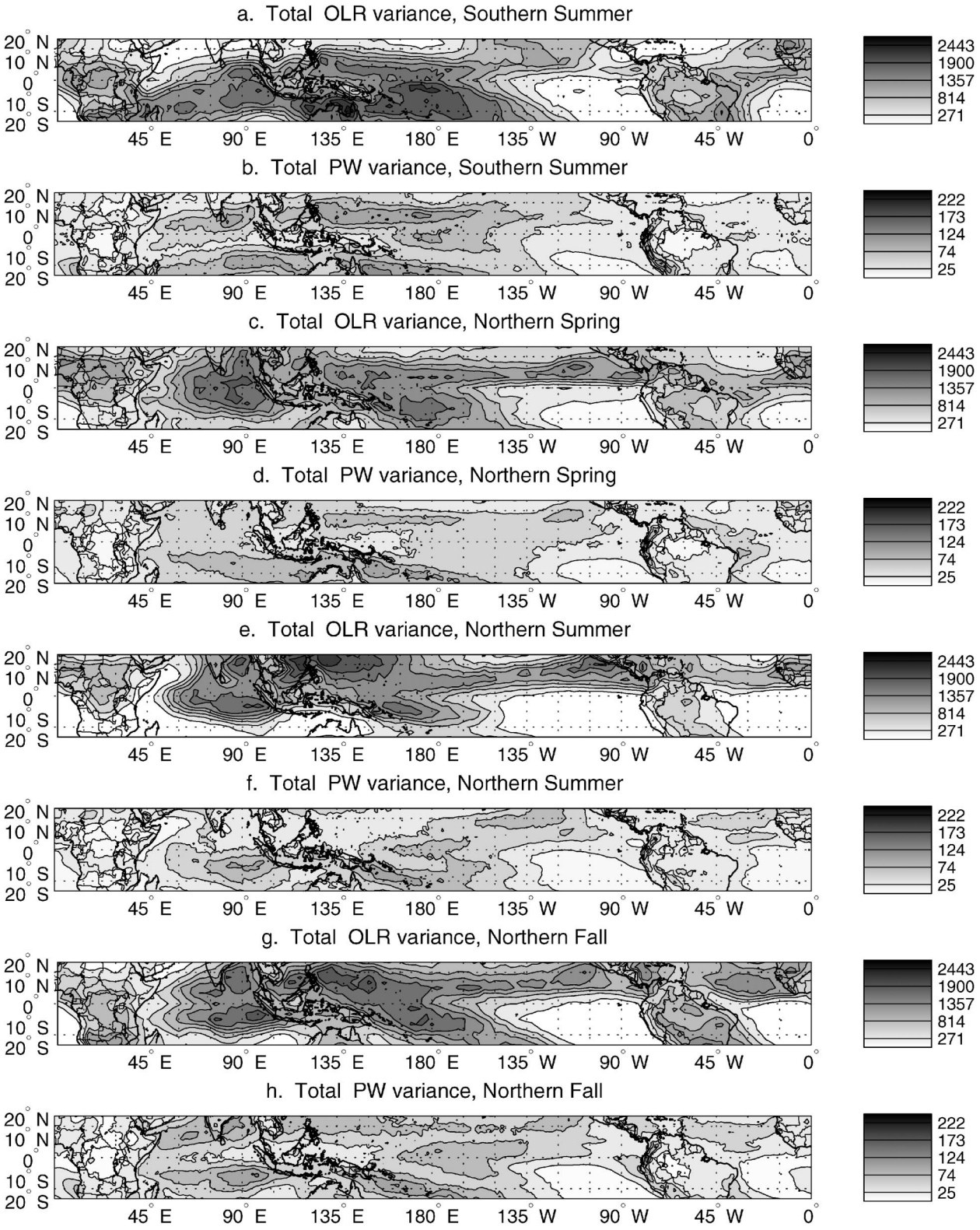

FIG. 6. Total variance of the OLR and PW anomalies, according to season after removing the annual cycle. Panels are arranged in seasonal pairs of OLR and PW [e.g., (a) and (b) represent the southern summer result for OLR and for PW, respectively].

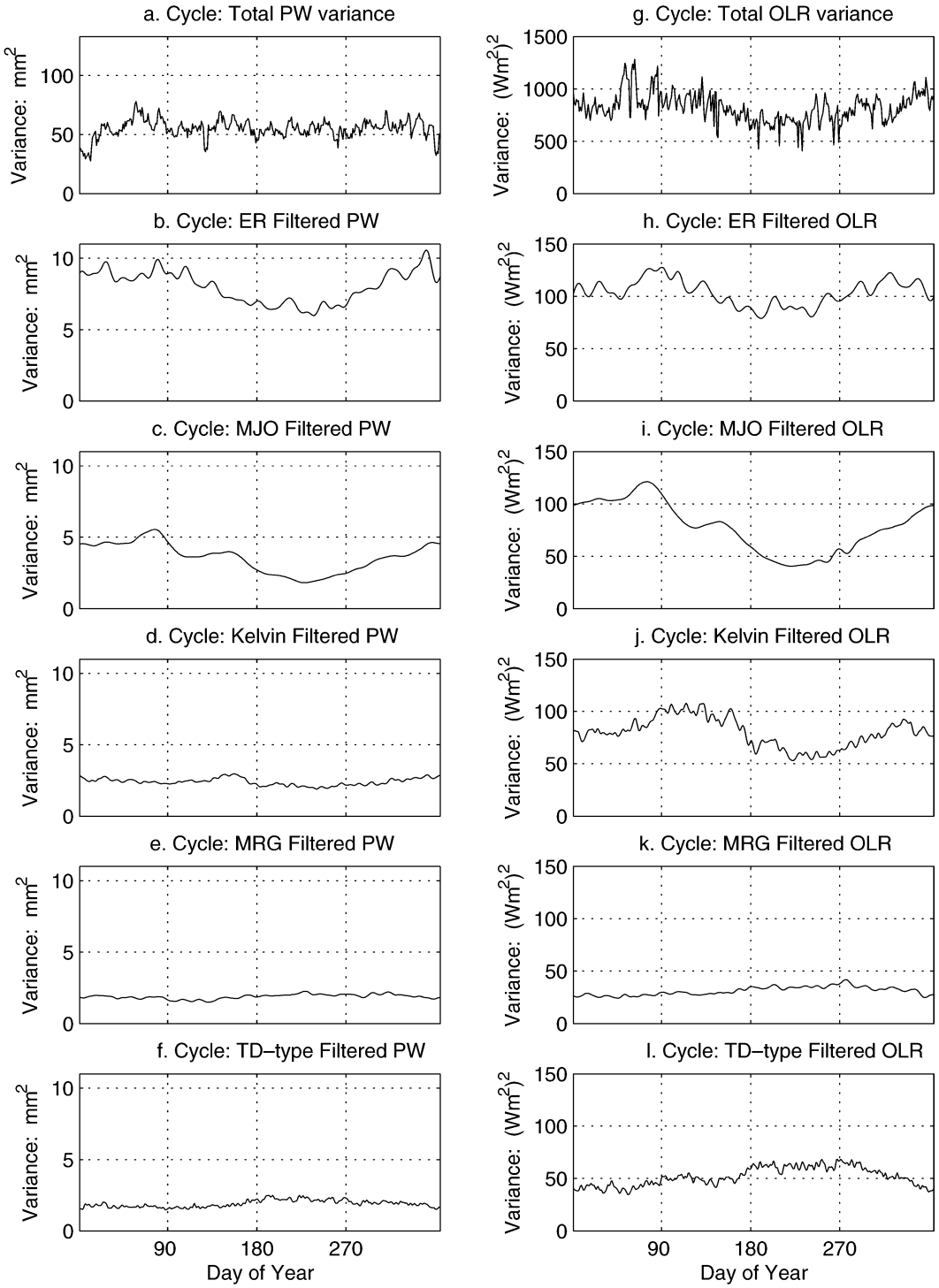

FIG. 7. Estimates of the annual cycle of variance (averaged from 20°N to 20°S) (top) for the raw PW and OLR anomalies and for each of the filter types. (a)–(f) The estimates for the PW data; (g)–(l) OLR.

that variance in the ER band may be greatest during transition seasons when solar insolation is symmetric across the equator. This filter band explains about 20% of the global PW variance and up to 12% of the global OLR variance.

4) ISOe BAND-FILTERED DATA

The ISOe band includes most of the large-scale portion of the 30–60-day MJO. Figure 11 represents a snapshot of ISOe-filtered OLR, PW, and winds. The event

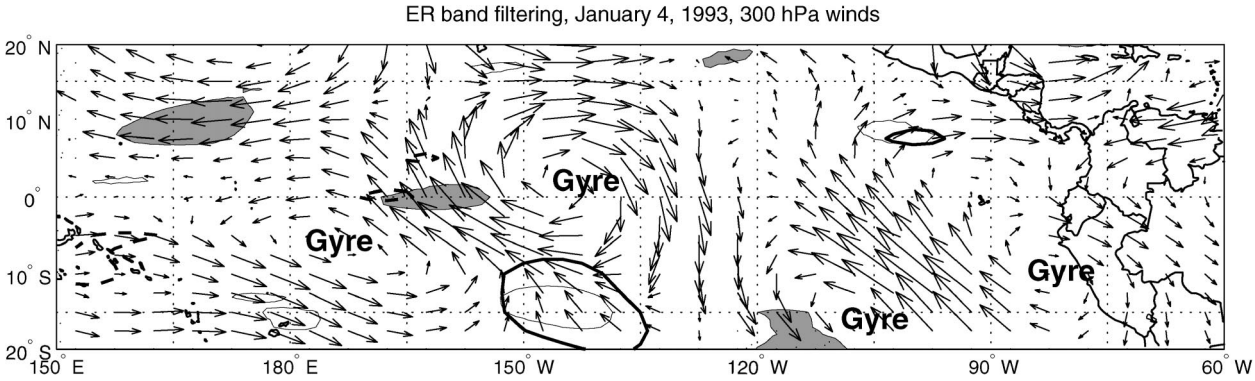

FIG. 8. Example map of ER band-filtered PW, OLR, and winds on 4 Jan 1993. Positive PW anomalies are shaded, and negative anomalies are fine contoured. OLR anomalies are given heavier contours, and their signs are generally opposite those of adjacent PW anomalies. Gyre or circulation centers are labeled.

shown here exhibits anomalously high PW and low OLR along the equator north and slightly east of Australia. West of this anomaly, an anomalous pattern of cross-equatorial flow is observed. East of the anomaly, a band of equatorial easterlies is flanked on the north and on the south by counterrotating gyres [consistent with the pattern seen in the composites of Hendon and Salby (1994)]. Figure 12 represents the segment of the ISOe band OLR and PW filtering result at 10°S. This latitude was chosen because it is close to the maximum variance latitude of ISOe band-filtered OLR and PW. Similar structures are visible in WK99's Fig. 11a, though their filter was narrower than ours. Positive OLR anomalies nearly align with negative PW anomalies, except that PW anomalies often lead OLR anomalies slightly.

The larger wavenumber width of our filter evidently adds structure to that of the WK99 result, because anomalies in our result appear to have slower phase speeds than the corresponding anomalies of WK99. These changes indicate that including the higher wavenumbers alters the structures of anomalies, providing evidence that a wavenumber-1–4 filter may not capture all of the important large-scale portions of the ISO process. Including higher wavenumbers in the filter appears to break up the continuity of propagating anomalies. Many individual anomalies shown in WK99 are shown as collections of multiple anomalies in our result. Anomalies near these breaks often take on standing character if westward propagation is included in the filter (not shown).

Three dominant ISOe variance regions are visible in both the OLR and PW ISOe variance maps in Fig. 13. These regions include a northern track between 10°N and 20°N, an equatorial track, and a southern track between 5°S and 20°S. The results of Roundy and Frank (2004a,b) reveal that three distinct envelopes of PW often propagate eastward together, occupying each of the three regions. Other studies that have analyzed OLR have related these three regions to the Northern Hemisphere intraseasonal oscillation (NHISO; Kemball-Cook and Wang 2001), but this behavior occurs throughout the year in the PW anomalies. Further analysis indicates that the off-equatorial anomalies are associated with a divergence pattern that is produced by Rossby gyres that are triggered by the release of latent heat in the strong convective anomalies of the ISOe.

The strongest ISOe signal occurs during the southern summer in the southern track between about 70°E and 140°W. The PW variance tracks during the northern summer and northern fall are zonally broader than those in OLR and extend farther east over the North Pacific.

Figures 7c and 7i present the annual cycle of variance of the ISOe. Precipitable water and OLR results are similar. Both peak during the southern summer, with a distinct minimum during the northern summer, consistent with the results of many others (e.g., Madden and Julian 1994).

5) KELVIN BAND-FILTERED DATA

The theoretical Kelvin wave is an eastward-propagating nondispersive disturbance of the zonal wind that peaks on the equator and produces a Gaussian wind distribution centered on the equator. WK99 and Straub and Kiladis (2002) showed that OLR anomalies associated with convectively coupled Kelvin waves are confined more closely to the equator than are ISOe anomalies. These Kelvin anomalies propagate at more than twice the speed of the eastern hemisphere ISOe. The horizontal snapshot of the Kelvin-filtered data is given in Fig. 14 (for 14 January 1993). The disturbance that appears in this figure that is most consistent with the theoretical Kelvin wave and the result of Wheeler et al. (2000) is centered at the point labeled C. Equatorial zonal winds converge about that point. The westerlies (labeled W) are strongest on the equator. The region of easterlies (labeled E) appears to be distorted from the expected zonal pattern. The equatorial PW anomaly associated with the wave appears to be centered closer to the equator than the 850-hPa wind disturbance. This PW anomaly is responding to more than just the 850-hPa

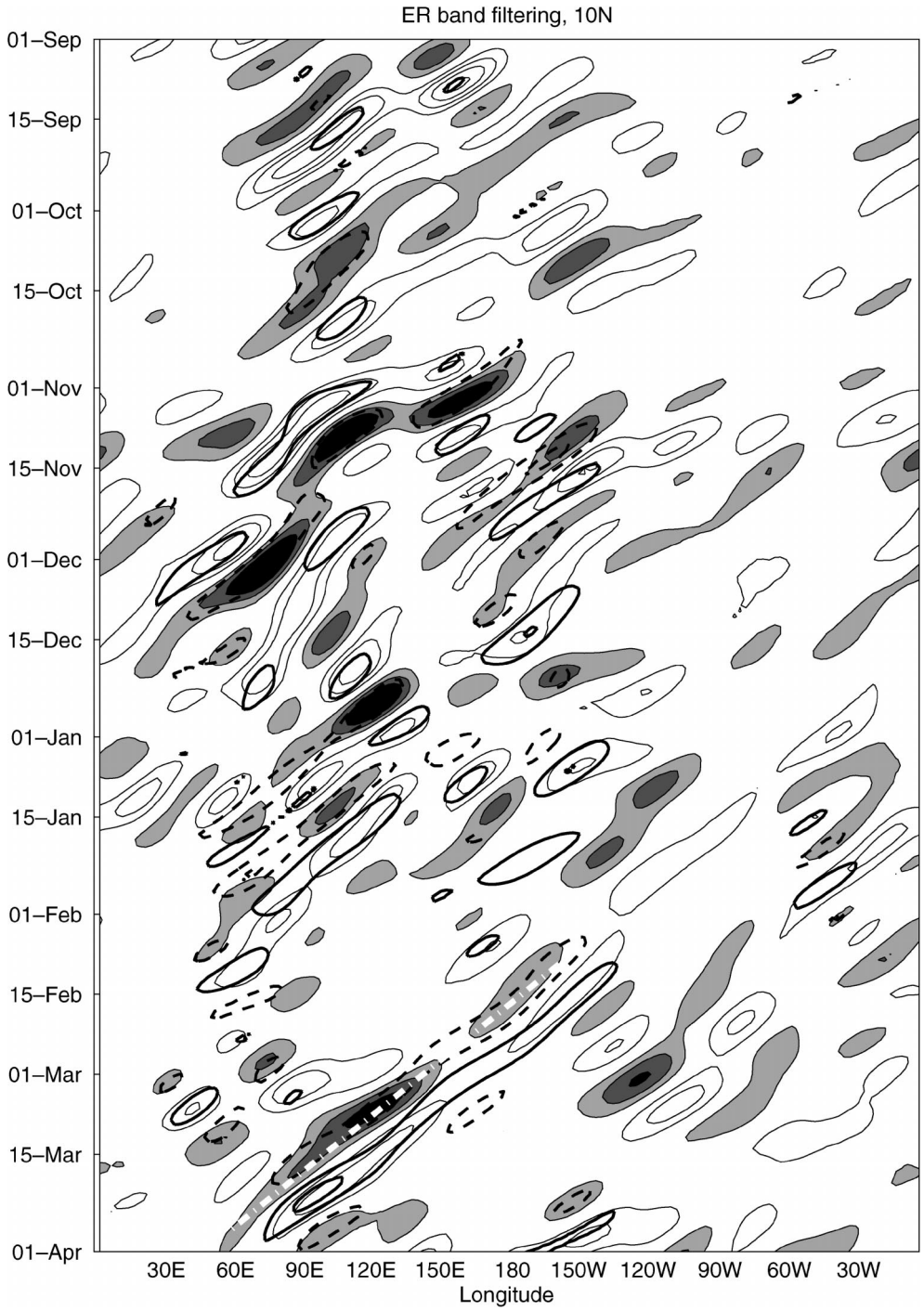

FIG. 9. Longitude–time diagram of ER band-filtered PW and OLR anomalies. Positive PW anomalies are shaded and negative anomalies are fine contoured. OLR anomalies are heavy contoured, and negative OLR contours are dashed. Contour intervals are 2.75 times the mean absolute anomaly of the entire 10-yr longitude–time matrix. This allows OLR and PW results to be objectively compared. The zero contour is omitted. The dashed–dotted white line centered approximately on 1 Mar represents the trajectory of an example ER anomaly. A similar line is plotted at the same location on Fig. 5, for comparison with the raw data.

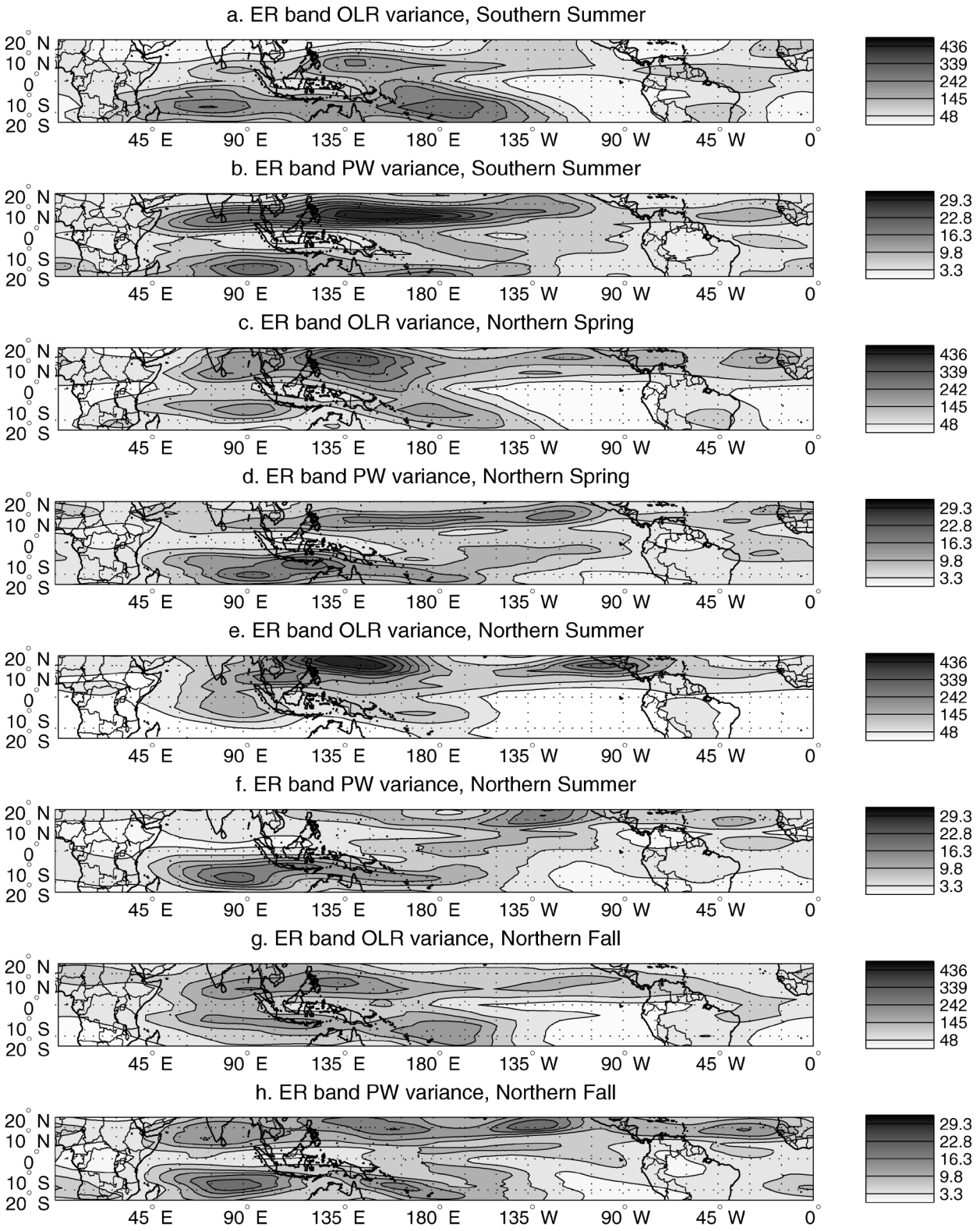

FIG. 10. Variance of ER band-filtered OLR and PW by season. (a), (b) the southern summer results for OLR and for PW, respectively; (c), (d) the same for northern spring; (e), (f) the result for northern summer; (g), (h) the northern fall.

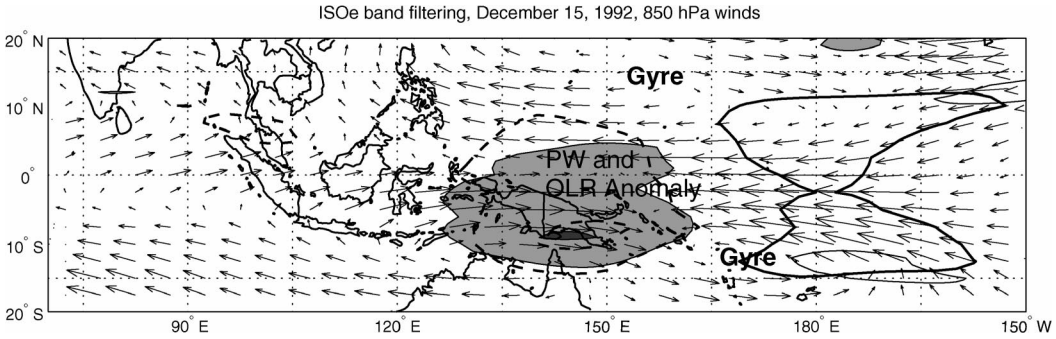

FIG. 11. Example map of ISOe band-filtered PW, OLR, and winds for 15 Dec 1992.

winds, so it is not fully consistent with the 850-hPa divergence pattern.

Figure 15 represents the segment of the Kelvin band OLR and PW result at 2.5°N. We selected 2.5° because convective anomalies that move from the Indian Ocean basin to the Pacific basin propagate along a line slightly north of the equator after they cross the date line in response to the equatorial pool of low SSTs, which suppresses moist deep convection. Straub and Kiladis (2002) discuss a case study of a Kelvin wave event that excited an asymmetric convective anomaly in the eastern Pacific basin while retaining the most of the more symmetric wind field characteristics of a Kelvin wave. Both their analysis and ours indicate that these waves often propagate continuously from the Indian Ocean and across the entire Pacific basin. Some events in our results appear to traverse the entire globe. Others appear to begin and end within the same basin.

Precipitable water anomalies in the Kelvin band often coincide with OLR anomalies of opposite signs, but PW anomalies usually lead. The phase shift may be due to forcing associated with the wave dynamics, or it may simply indicate that the atmosphere tends to moisten prior to the onset of moist convection as found by Straub and Kiladis (2002, 2003c). It may also indicate the tendency of the OLR signal to lag the deep convection somewhat because of its strong sensitivity to cirrus left behind by the convection. The phase difference between related OLR and PW anomalies does not always remain constant with time. Precipitable water anomalies always lead OLR anomalies where anomalies are growing with time, and OLR anomalies occasionally lead where anomalies decay. Although these data are filtered to highlight Kelvin waves, some of the off-equatorial PW anomalies in these Kelvin band-filtered data are actually associated with extratropical Rossby waves that are advected eastward by seasonal westerly winds. Straub and Kiladis (2002) mention these waves in their analysis. Some of these waves appear to trigger and occasionally remain in phase with the equatorial Kelvin waves (see Straub and Kiladis (2003a). These waves also appear (to a lesser extent) in OLR.

Figure 16 confirms that OLR and PW both trace convectively coupled Kelvin waves, but it also confirms [along with the spectra (Figs. 2–3)] that OLR is a better tracer of these waves. The weak PW Kelvin wave variance track (near the equator) does align well with a similar OLR variance track. The above-mentioned off-equatorial waves dominate the poleward edges of the domain, especially in the winter hemisphere. The near-equatorial variance peak confirms our observation from the Hovmoeller diagrams that PW and OLR anomalies that are associated with Kelvin waves often propagate along the equator toward the date line, then move northward to between 2° and 4°N where they resume propagating parallel to the equator. When this shift occurs, the Kelvin wave may be marginally symmetric, but the axis of symmetry is displaced north of the equator.

Figures 7d and 7j give the annual cycles of variance for Kelvin band-filtered PW and OLR, respectively. This result shows that only about 5% of the total variance of PW is contributed by this band. Kelvin band OLR variance peaks during northern spring with a secondary peak during northern fall. The minimum occurs during northern summer. The Kelvin band makes up about 10% of the total tropical OLR variance during northern spring, and about 7.5% during northern summer.

6) MIXED ROSSBY–GRAVITY BAND-FILTERED DATA

Theoretical MRG waves (meridional mode $n = 0$) consist of vortices centered on the equator with divergence profiles that are antisymmetric across the equator. Figure 17 represents a horizontal snapshot of MRG band-filtered data, showing a wave train in the Pacific basin consisting of gyres centered near, but not exactly on the equator. The vortex located farthest west is centered north of the equator. This wave train is similar to (but larger in spatial scale than) the case study of a wave train discussed by Dickinson and Molinari (2002). The wave train (in Fig. 17) only excited significant OLR and PW anomalies north of the equator in and near the expected position of the ITCZ. An analysis of antisymmetric-filtered OLR (not shown) does not reveal this event, yet its wind field structure is clearly similar to that of an MRG wave.

Further analysis of maps such as Fig. 17 reveals that another, largely asymmetric waveform also occurs in

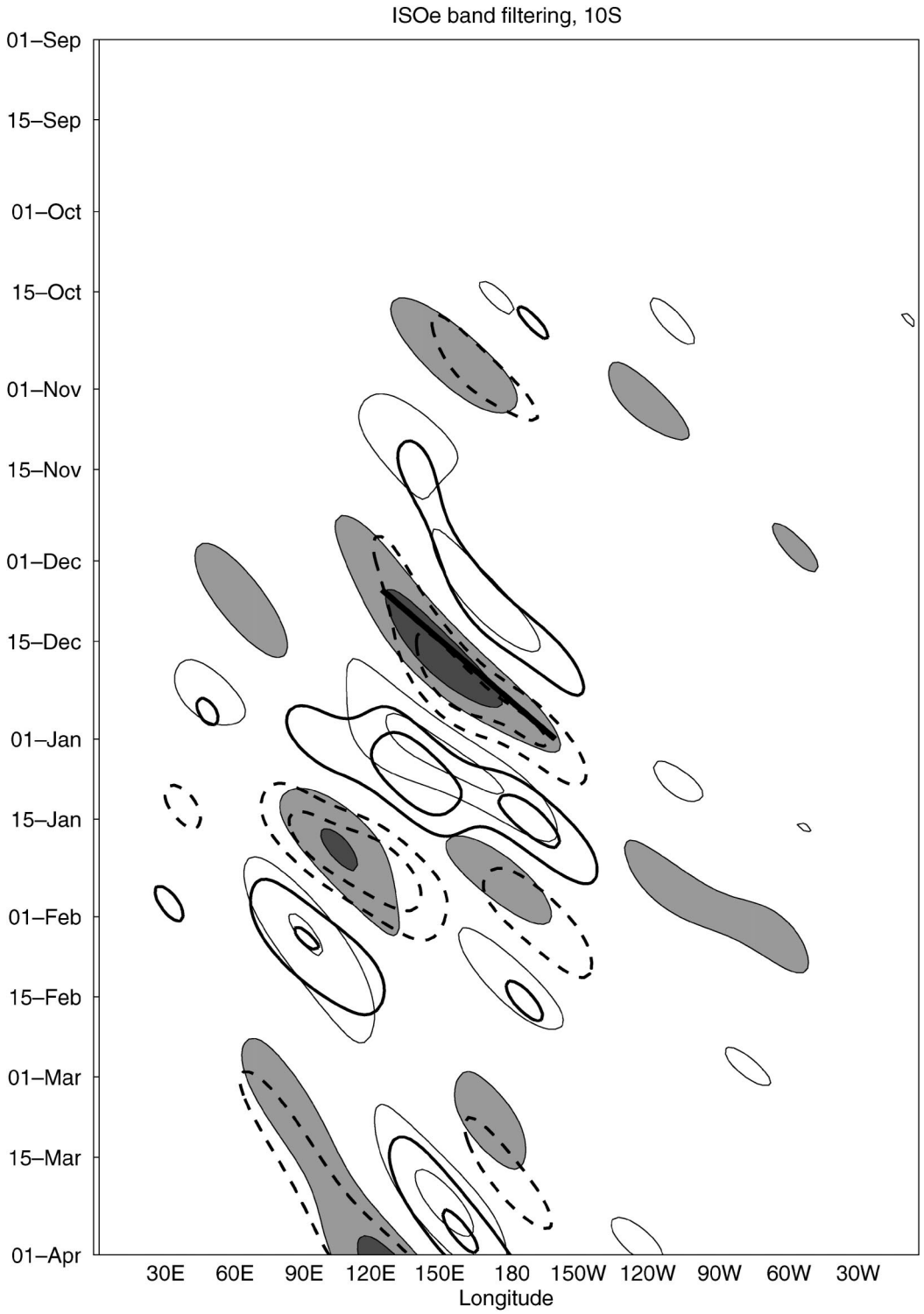

FIG. 12. Longitude–time diagram of ISOe band-filtered OLR and PW anomalies, formatted as discussed in the caption of Fig. 9. The solid line centered west of the date line and near 15 Dec approximates the trajectory of an active MJO anomaly, and a similar line is drawn at the same location in Fig. 5 for comparison.

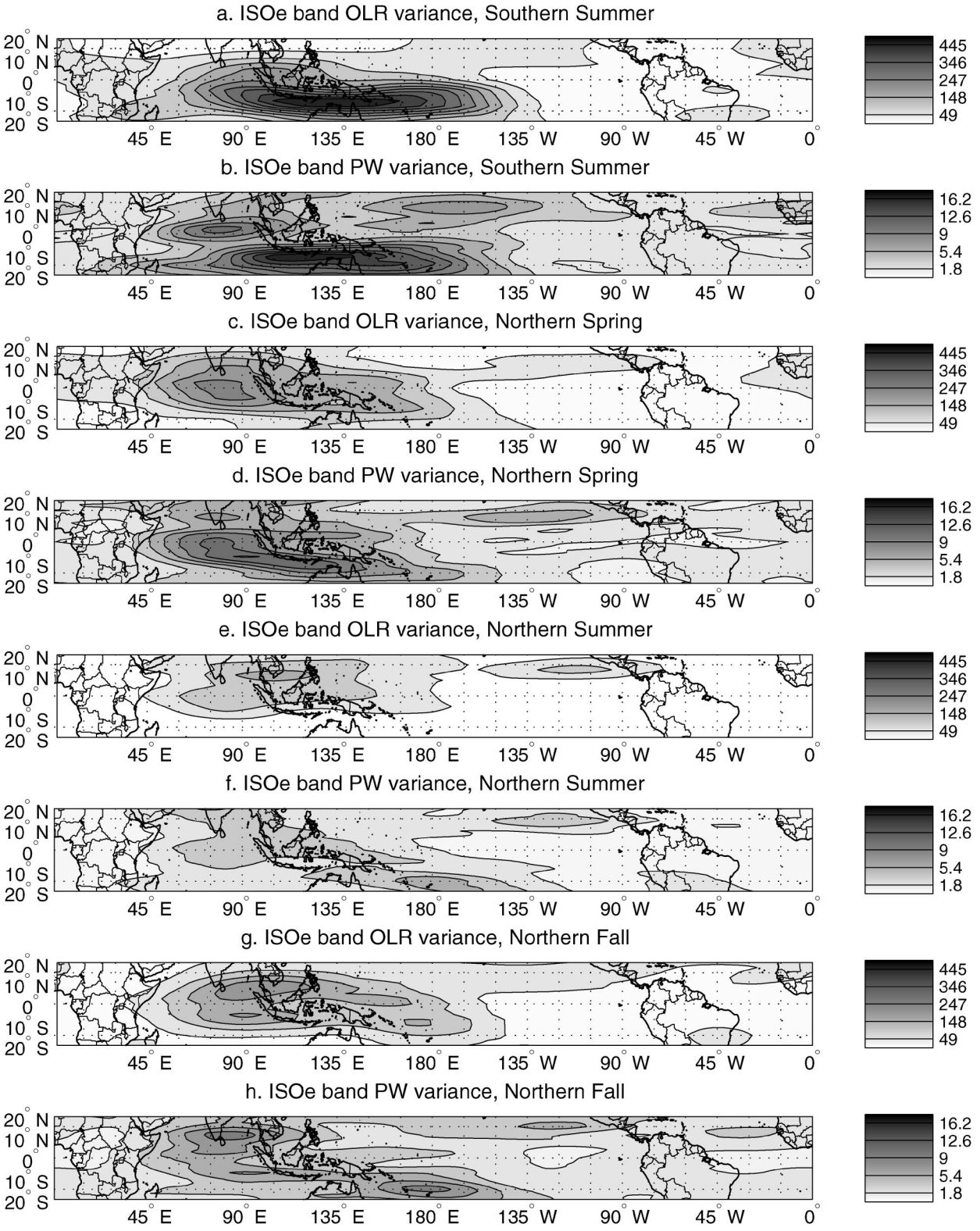

FIG. 13. Seasonal maps of OLR and PW variance in the ISOe band. Formatting is similar to that in Fig. 10.

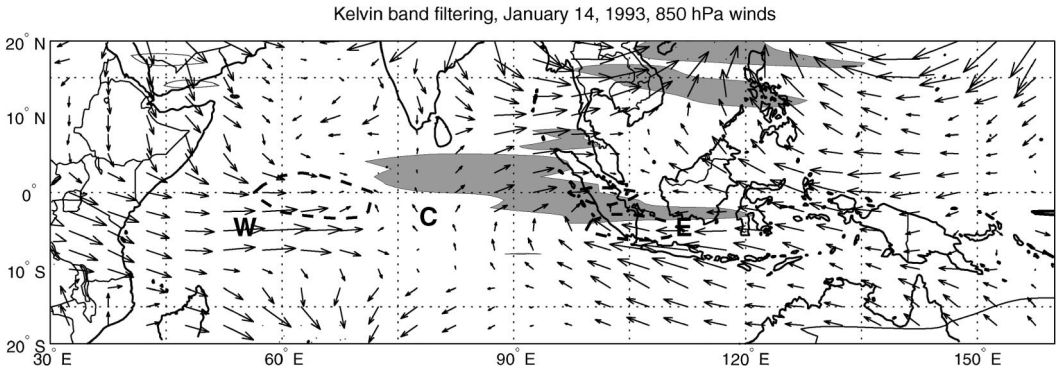

FIG. 14. Example map of Kelvin band-filtered PW, OLR, and winds for 14 Jan 1993. Formatting is similar to that in Fig. 8. The labels E, C, and W are placed in regions of easterly winds, zonal convergence, and westerly winds that together form a pattern that is roughly consistent with the structure of the linear Kelvin mode.

this band. These latter waves behave somewhat like large TD-type disturbances or easterly waves. Other waveforms that appear in the MRG band-filtered data are symmetric across the equator, with structures similar to $n = 1$ ER waves with high equivalent depths. The spectra indicate some overlap between the peaks associated with MRG waves, TD-type disturbances, and Rossby waves, so some of the waves in this filter band are actually associated with those wave types (e.g., the gyre near 150°E in Fig. 16 is centered north of the equator, like a large TD-type disturbance). In spite of these different patterns, most of the stronger anomalies that occur in one hemisphere are coupled with anomalies of opposite sign in the other hemisphere. Anomaly amplitudes in the Northern Hemisphere are usually larger than those in the Southern Hemisphere. The signal is most likely to produce antisymmetric anomalies during northern fall (e.g., Liebmann and Hendon 1990; Hendon and Liebmann 1991).

Figure 18 is the Hovmoeller diagram of the MRG filter band segment at 7.5°N. Our OLR result is nearly identical to that of WK99. Precipitable water appears to be more sensitive to waves in the MRG spectral range than is OLR. As in the results for the other filters, PW anomalies often lead OLR anomalies in time. These results also indicate that the disturbances in the spectral range of MRG waves exhibit an eastward group velocity, consistent with shallow water theory.

Variance maps of MRG bandpass-filtered OLR and PW are given in Fig. 19. Maximum OLR variance occurs during the northern summer and in the Northern Hemisphere. The greatest PW variance occurs in the Northern Hemisphere during southern summer, when advection across strong meridional PW gradients generates high-amplitude anomalies. Asymmetries are apparent in both OLR and PW variance, with the greatest variance usually occurring in the Northern Hemisphere, except during the northern and southern summers in the Indian Ocean basin. Nearly global bands of high variance occur in the Northern Hemisphere, but in the Southern Hemisphere there is little variance over the East Pacific or Atlantic basins. The PW variance maps appear to discern two tracks of variance in each hemisphere during northern fall, including one pair along 7.5°N and 7.5°S and another between 10° and 20° in both hemispheres. These bands are most visible just east of the date line, and they occur at the north and south edges of the band of active OLR variance.

The annual cycle estimate for MRG band-filtered PW is almost constant throughout the year, accounting for just less than 5% of the total variance (Fig. 7). The result for OLR has a broad maximum at the end of the northern summer and the beginning of the northern fall. The annual cycle of variance for the MRG filter is similar to that for the TD-type filter (discussed later), but the MRG band actually generates less of the total variance than the TD-type filter band. The OLR and PW signals are concentrated in the north Pacific ITCZ region, where the same annual cycle processes may affect them.

7) TD-type band-filtered data

TD-type disturbances consist of anomalous westward-propagating vortices located poleward of the equator that usually occur as asymmetric waves. Some of them occasionally develop warm cores and form tropical cyclones. This wave type has long been known to be common in the Atlantic basin during northern summer, where disturbances often originate from instabilities in the region of the African easterly jet (e.g., Carlson 1969). An example horizontal snapshot of a train of such disturbances in the filtered OLR, PW, and winds, is shown in Fig. 20. The TD-type disturbance is not the only source of variability that occurs in this filter band. Disturbances in this band are also occasionally produced by equatorially trapped modes. The band is relatively quiet in the North Atlantic basin during the northern winter, when significant anomalies still occur in the Pacific basin and in the Atlantic basin close to the equator.

Figure 21 gives an example global snapshot of the TD-type band-filtered data for 7 December 1992. In this

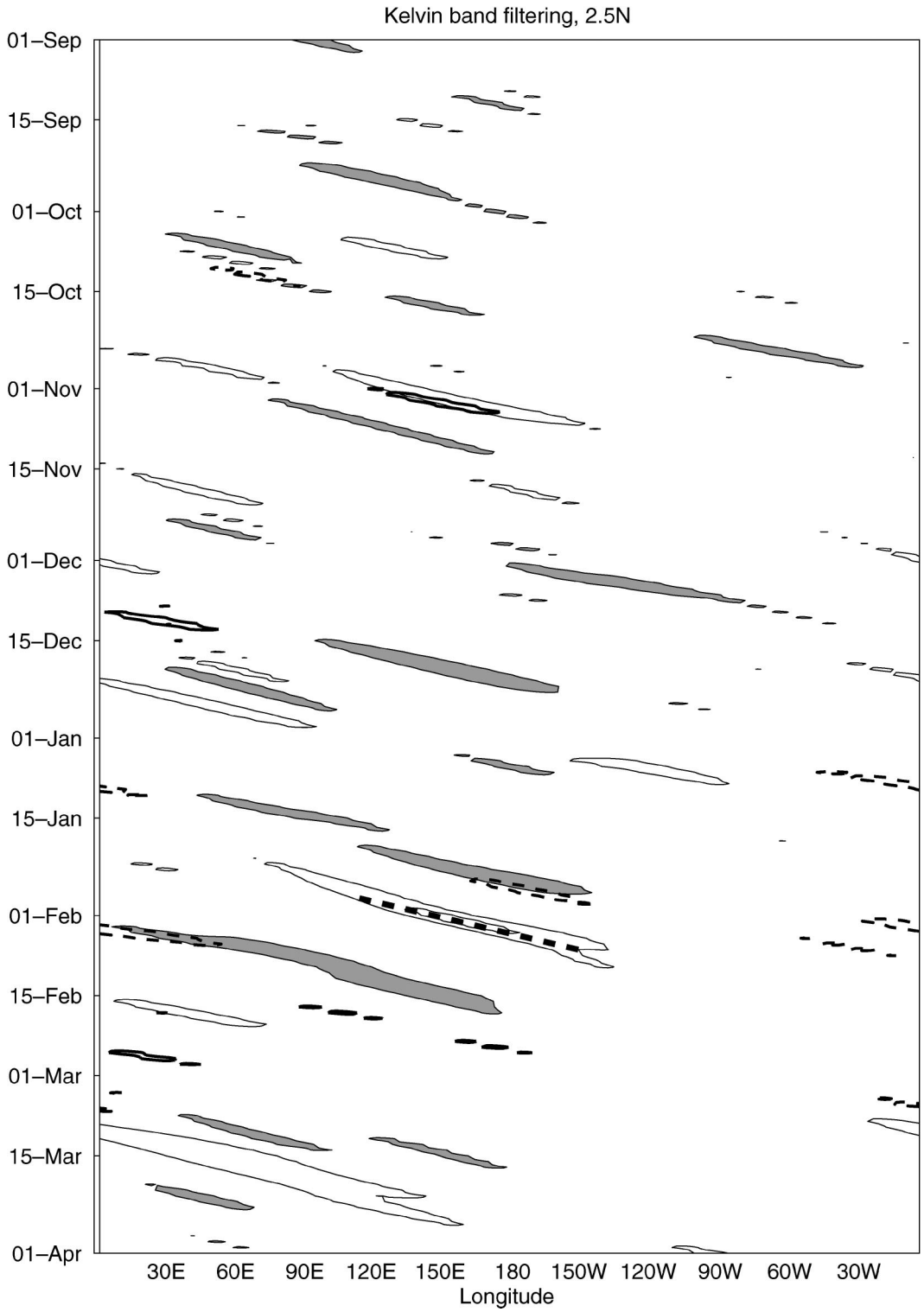

FIG. 15. Longitude–time representation of Kelvin band-filtered OLR and PW, formatted as in Fig. 9. The heavy dashed line centered before 1 Feb and west of the date line traces a negative Kelvin band PW anomaly, and it is given to facilitate comparison with Fig. 5. Note that the meridional averaging used in Fig. 5 reduces the amplitudes Kelvin anomalies relative to the amplitudes of anomalies of other waves.

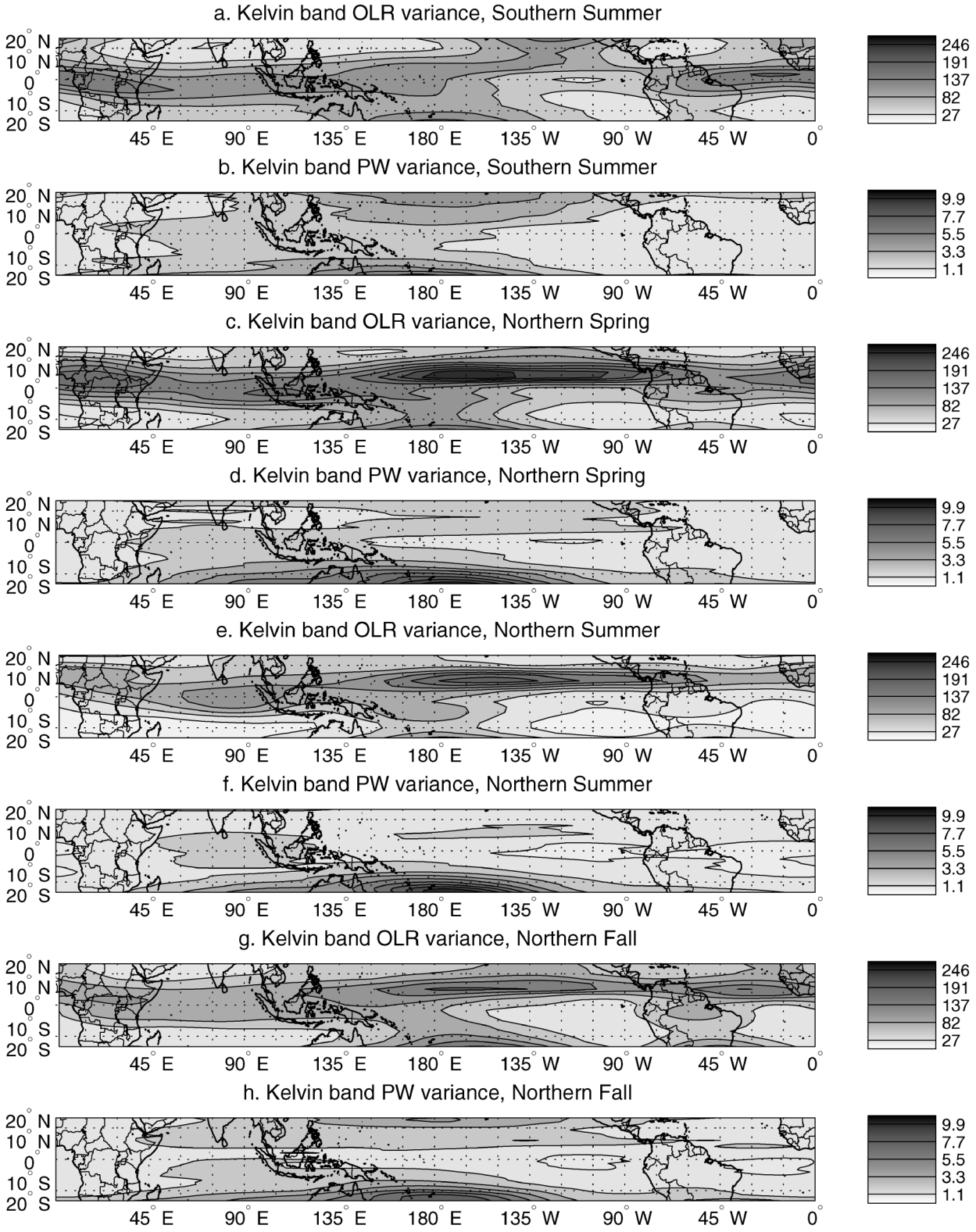

FIG. 16. Seasonal maps of OLR and PW variance in the Kelvin band. The figure is formatted similarly to Fig. 10.

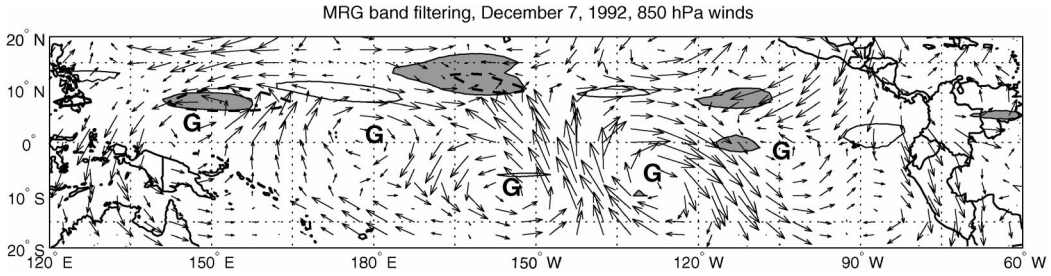

FIG. 17. Map of MRG band-filtered PW, OLR, and 850-hPa winds, formatted similarly to Fig. 8. The label G is placed near the centers of prominent gyres.

example, a set of gyres (similar to a high-wavenumber MRG wave train) is propagating westward along the equator. These gyres appear to perturb the region of the weak North Pacific ITCZ (Figs. 2a and 2b), forming positive and negative OLR/PW anomaly pairs north and south of the mean location of the ITCZ. These patterns differ from the structure of a TD-type disturbance because the vortices are centered close to the equator instead of farther poleward. The convective pattern also differs from the theoretical divergence pattern associated with an MRG wave, because the anomalies are antisymmetric across the ITCZ instead of across the equator.

Figure 22 shows a TD-type band-filtered segment at 7.5°N. There is a period of activity in this band in the Atlantic basin during September, but this basin is relatively quiet during the remaining months shown. A much longer period of higher-amplitude wave activity occurs between about 160°E and 120°W. These latter disturbances propagate westward in the Pacific ITCZ and are active during October through late December, with the strongest activity occurring during October. Precipitable water appears to be more sensitive to these waves than OLR, presumably because they induce meridional winds that traverse regions of high PW gradients adjacent to the ITCZ.

Figure 23 shows the seasonal variance estimates of TD-type band-filtered OLR and PW. The greatest variance in this band occurs during the northern summer in the central and western Pacific basin near 7°–10°N. Consistent with previous research (e.g., Carlson 1969; Gu and Zhang 2001), activity in the Atlantic basin is part of a broad region of high variance that begins over Africa, especially during the northern summer. These results reveal that variance in the North Pacific basin often occurs with a mirror track of variance in the Southern Hemisphere. Many of the waves that contribute to these patterns are similar to the high-frequency MRG waves discussed above, except that these occasionally produce antisymmetric cross-equatorial patterns. The annual cycle estimates for variance in this filter (Figs. 7g and 7k) confirm that this filter band is globally most active during the northern summer and fall.

4. Conclusions

This work extends that of WK99 by presenting a seasonal climatology of the wavenumber–frequency bands of five of the most important propagating modes in the tropical atmosphere. It reveals where and when the modes are most active. It also suggests that linear equatorial beta-plane shallow water theory is insufficient to explain much of the behavior of tropical waves and oscillations. Convective anomalies that are enhanced by the waves do not generally follow patterns predicted by the linear theory for divergence forced by dry waves. Instead, the waves appear to enhance or suppress base-state convection and interact with it. The waves then interact with other waves, with background winds, and with topographical features (e.g., Roundy and Frank 2004a,b). The result is OLR and PW patterns that contain asymmetric parts with respect to the equator. Understanding and acknowledging these asymmetries is important to weather forecasting in the Tropics.

Results show that filtering in the wavenumber–frequency domain is useful for isolating modes, even though each filter band contains multiple modes because their spectra overlap. The filter bands discussed here have been shown to be locally important in many regions where they sometimes contribute most of the variability (excluding the annual and diurnal cycles).

Precipitable water appears to trace wave activity more effectively than OLR through the western hemisphere (e.g., Fig. 5). Precipitable water is also more sensitive to waves that produce meridional advection across regions of strong PW gradients. Such waves include equatorial Rossby waves, mixed Rossby–gravity waves, and TD-type disturbances. Mixed Rossby–gravity waves appear less antisymmetric in PW anomalies than they do in OLR anomalies, as shown by the spectra (Figs. 3 and 4). Precipitable water is a poorer tracer of Kelvin waves than OLR. Thus, a climatology based both on OLR and PW data is more complete than a climatology based on only one dataset.

Results indicate that the ISOe and Rossby wave bands contribute more to the total variance of convection and moisture in the Tropics than other bands (e.g., up to 20% of the global tropical PW variance or about 15%

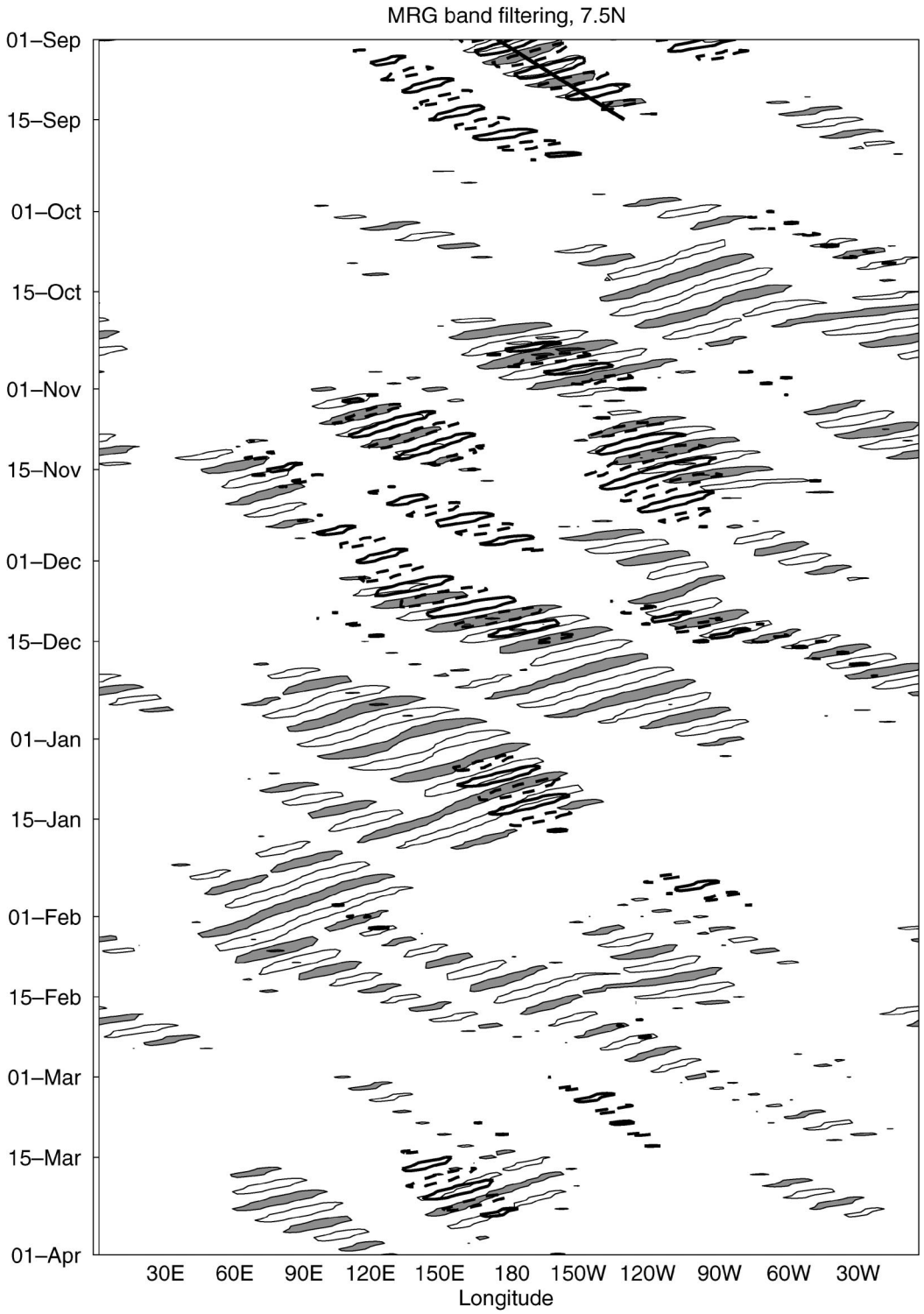

FIG. 18. Longitude–time representation of MRG band-filtered PW and OLR, centered at 7.5°N. Formatting is similar to that in Fig. 9. The solid black line centered in early Sep near the date line approximates the trajectory of a group of anomalies. A similar line is drawn at the same location on Fig. 5 to facilitate comparison with the raw data.

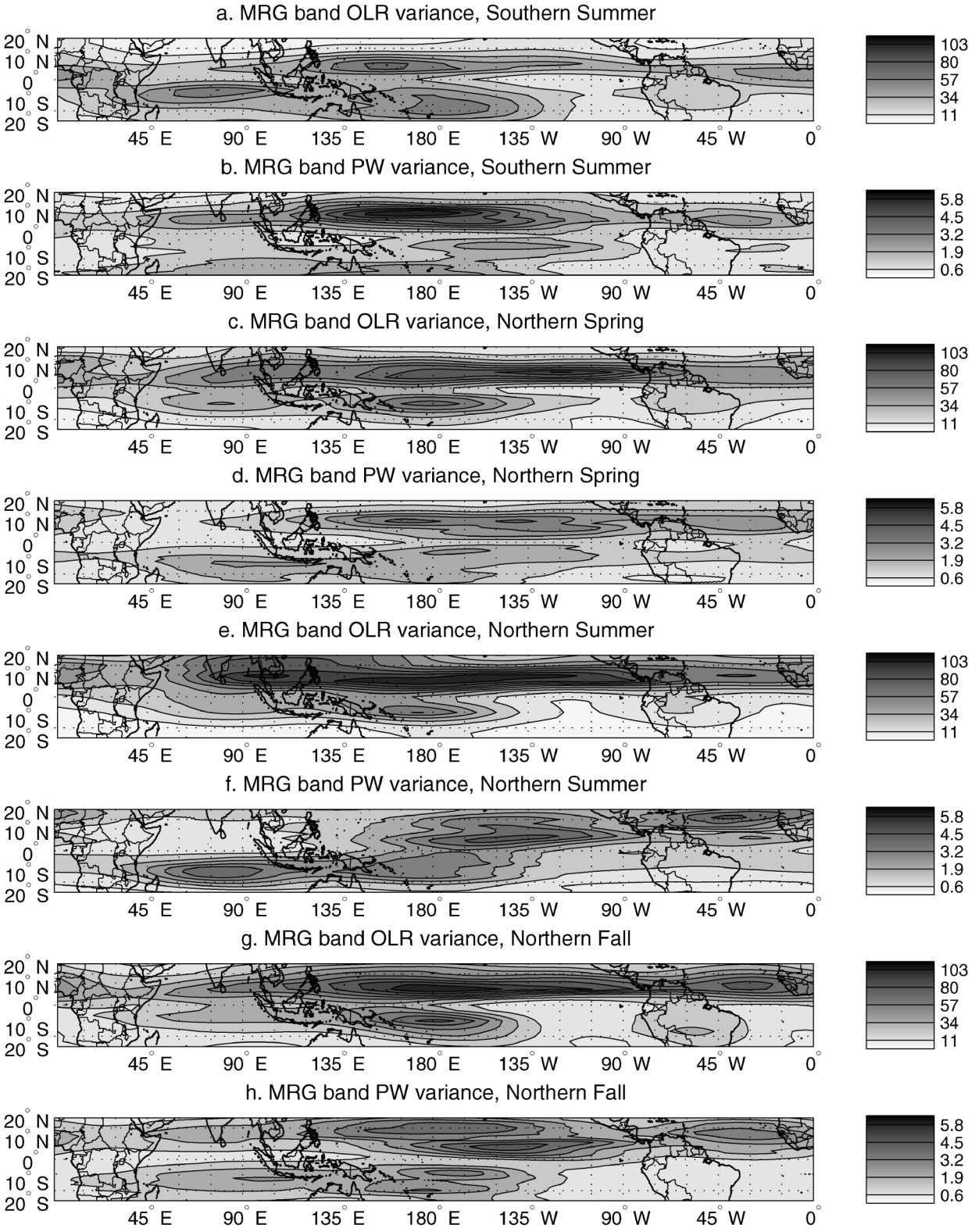

FIG. 19. Seasonal variance maps of MRG band-filtered OLR and PW. The figure is formatted similarly to Fig. 10.

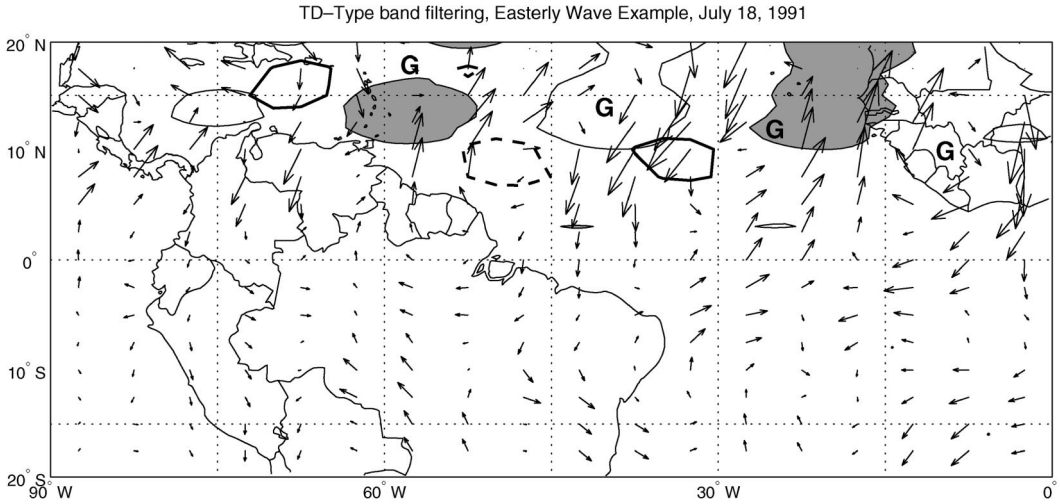

FIG. 20. Example map of an easterly wave train over Africa and the Atlantic basin, from TD-type band-filtered PW, OLR, and 850-hPa winds.

of the global tropical OLR variance). Locally the percentage of the total variance that occurs in these bands is much bigger. These bands contribute up to half of the local synoptic and planetary scale (less than wavenumber 16) OLR and PW variance in some regions. The TD-type band also contributes substantially to variance in the North Atlantic basin during the northern summer, where it contributes at least 15% of the local OLR and PW variance, or at least 40% of the OLR variance that is attributable to synoptic and planetary scales. The Kelvin band produces at least 20% of the local variance of convection near the equator and along the North Pacific ITCZ during northern spring (or at least 30% of the OLR variance of planetary- to synoptic-scale modes). The results imply that these modes may contribute similar proportions of local rainfall throughout the Tropics, and we will explore this in a future study. These wave modes may also contribute to the weather by affecting tropical cyclogenesis (e.g., Dickinson and Molinari 2002), and we are currently pursuing research in this area.

Acknowledgments. This work was funded by grants from the National Science Foundation, ATM 0003351 and ATM 0233881, and by a supplemental fellowship from the NASA Pennsylvania Space Grant Consortium. This paper was adapted from the Ph.D. thesis work of Dr. Roundy. Comments from his doctoral thesis committee were helpful, along with feedback from Dr. George Kiladis.

APPENDIX

Wavenumber–Frequency Spectra

The purpose of this appendix is to discuss how the spectra shown in Figs. 3 and 4 were calculated. To begin the spectral analysis, the annual cycle was found at each grid point by smoothing a series of averages for each day of the year. This annual cycle was removed to make a set of anomalies. The anomalies at each latitude were then sorted into 60 zonally global 97-day time segments that consecutively overlapped each other by 65 days. The temporal mean and linear and quadratic trends were removed from each segment to eliminate signals with frequencies less than or equal to 1/97 cycles per day. The ends of the segments were tapered in time by cosine bells (a Hanning window) to minimize spectral leakage.

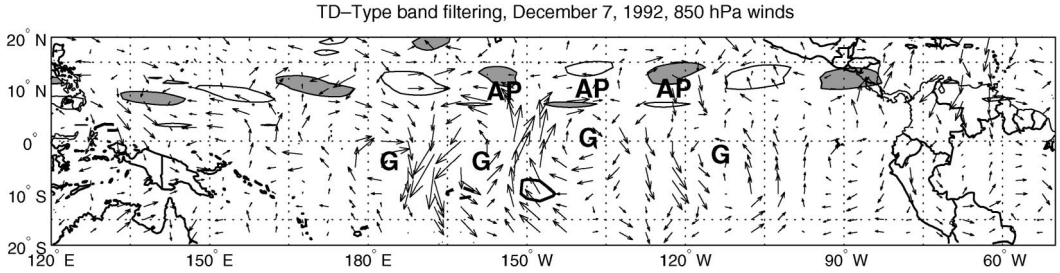

FIG. 21. Map of TD-type band-filtered PW, OLR, and 850-hPa winds for 7 Dec 1992. The label G is placed at the center of prominent gyres, and the letters AP label PW anomaly pairs situated on opposite sides of the weak Pacific ITCZ.

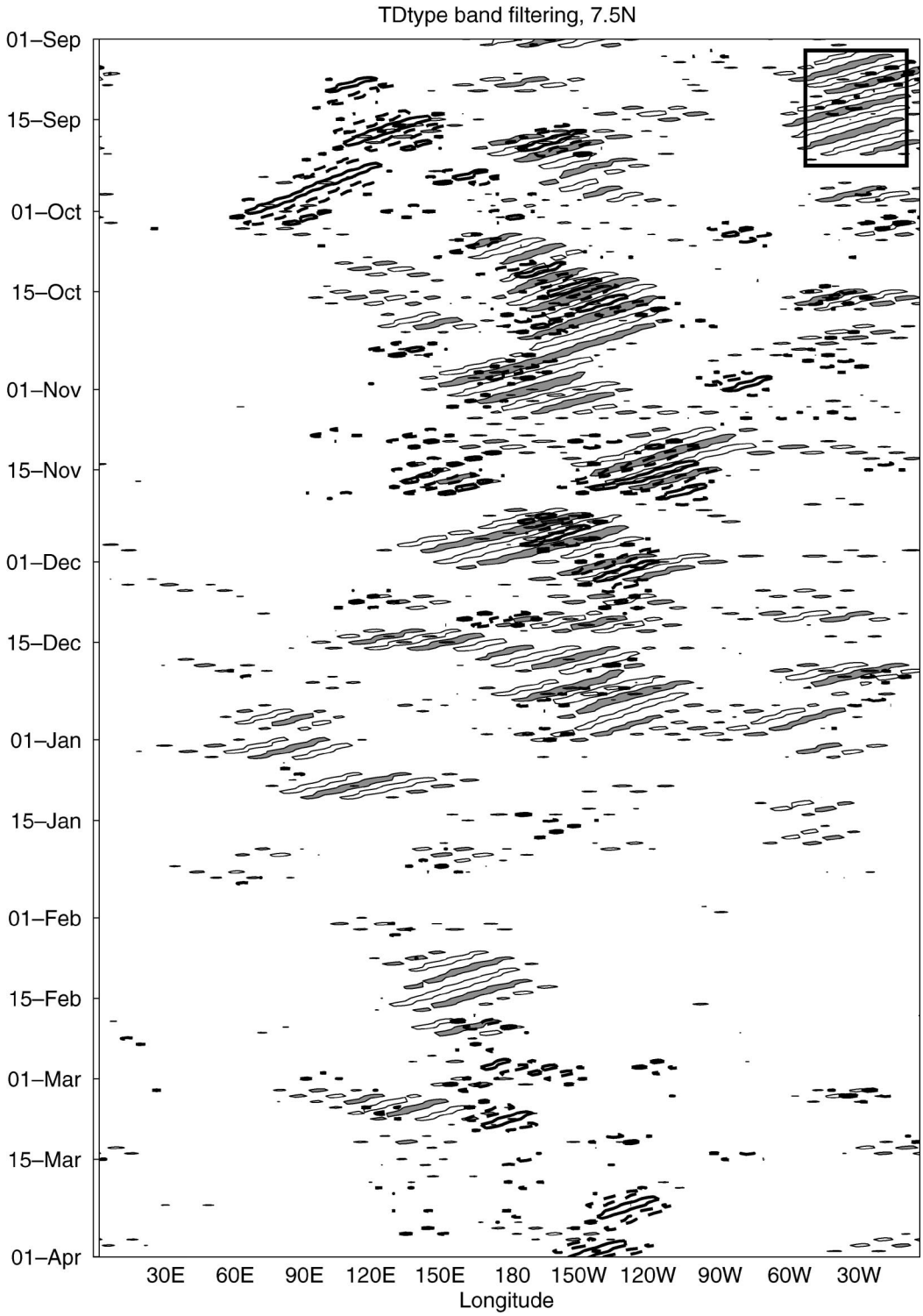

FIG. 22. Longitude–time representation of TD-type band-filtered PW and OLR, formatted as in Fig. 9. The rectangle drawn on the top right corner encloses an active period over the Atlantic basin, and a similar rectangle is drawn on Fig. 5 to help the reader compare the filtered and unfiltered data.

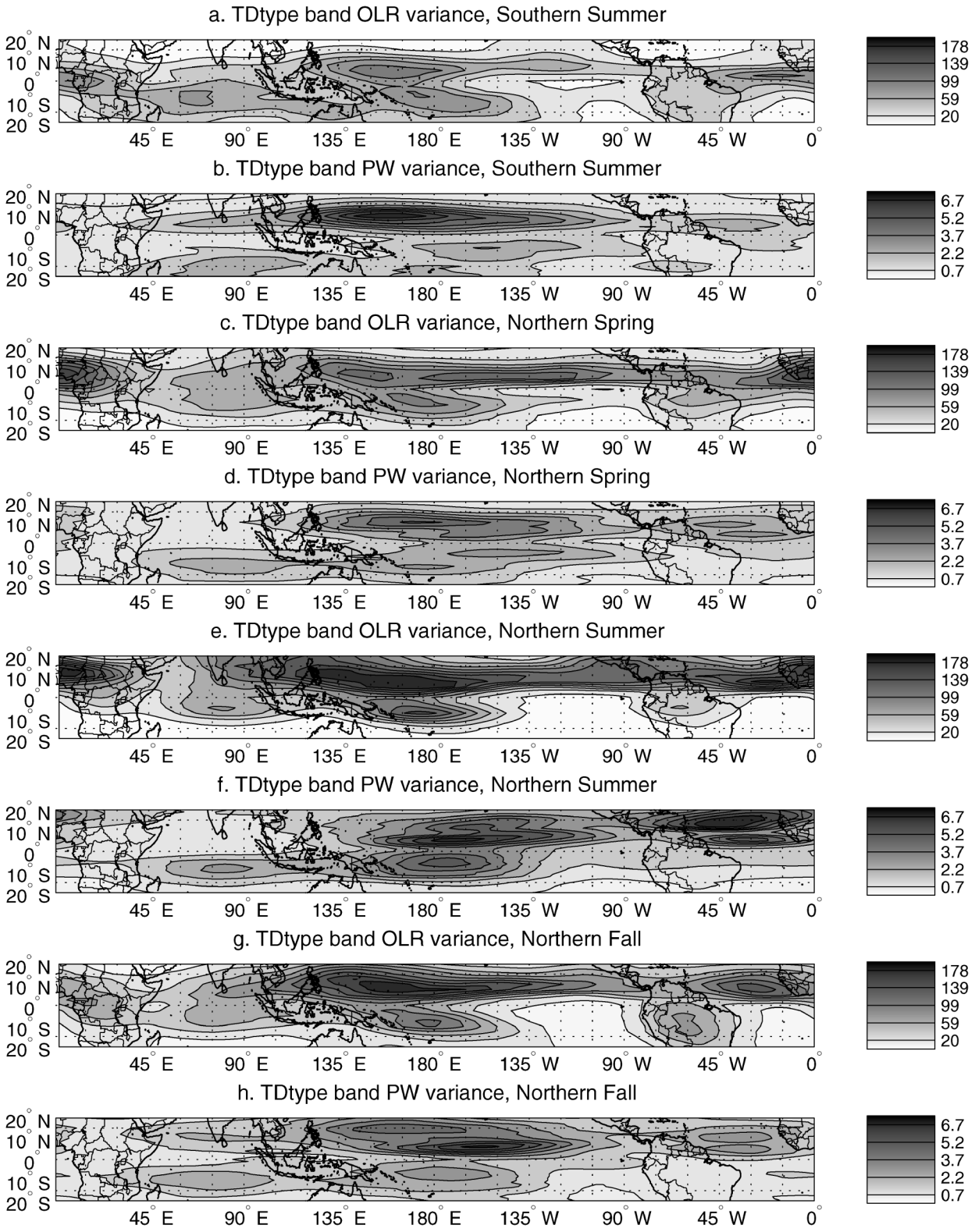

FIG. 23. Seasonal maps of variance of TD-type band-filtered OLR and PW, formatted as in Fig. 10.

The 97-day segment length was sufficient to analyze most synoptic- and planetary-scale waves having up to intraseasonal periods. The 65-day overlap recovers data lost by the tapering. As in WK99, results do not appear to be sensitive to the length of this overlap. The zonal space–time spectral estimates for each segment were calculated by decomposing the segments into complex wavenumber and frequency components for eastward and westward-propagating disturbances (Hayashi 1982) by means of a discrete Fourier transform in space followed by another in time, and then finding the product of this decomposition and its complex conjugate. The resulting power was then averaged over all available segments and all applicable latitudes or latitude combinations according to the desired spectrum format (discussed later). Only arrays representing data from 15°N to 15°S were included in the spectrum analyses (consistent with WK99). After finding the raw spectra, we applied a point-by-point statistical normalization of the spectra (discussed below) to account for the statistical stability of spectral peaks, instead of dividing by the background as done by WK99. The normalization allows the OLR and the PW results to be read on the same scale, and resulting values are nearly proportional to statistical significance above the background.

All spectra were calculated as follows. Let x represent the set of all segments included in a given spectrum type. A common background spectrum X (defined later), an appropriate standard deviate s, and an assumed Gaussian distribution of all segments were needed to normalize the spectra. The Gaussian assumption is acceptable for this case because the computation includes 300–400 degrees of freedom (DOF, as approximated by WK99), and histograms appear to be normally distributed. The standard deviate for a point in a given spectrum type is defined:

$$s = [\overline{(x - \overline{x})^2}]^{1/2}, \tag{A1}$$

where the overbars denote means. The spectrum-type specific mean standard anomaly z above the background was calculated:

$$z = \frac{\overline{x} - X}{s}. \tag{A2}$$

The normalized value N of the spectrum was then found by numerically integrating the standard Gaussian distribution from negative infinity to the mean standard anomaly for that point:

$$N = \int_{-\infty}^{z} \frac{1}{2\pi} e^{-y^2/2}\, dy. \tag{A3}$$

This normalization technique accounts for the statistical stability of spectral peaks and allows the PW and the OLR results to be read on the same scale.

The background spectrum X is defined to be the average of the symmetric and the antisymmetric spectra smoothed 40 times in wavenumber and frequency with a 1-2-1 filter, similar to the background used by WK99, but smoother. This 1-2-1 smoothing conserves integrated spectral power. This background spectrum may be analogous in some respects to the spectrum of random, nonperiodic, and nonsinusoidal signals in the data (WK99). Obviously, this background approximation contains more power than a true background of random processes because it contains the power of the waves as well. This implies that broad but shallow peaks associated with physical processes may be deemed insignificant by this procedure. Additionally, all background-smoothing methods of this type are subjective because the optimal amount of smoothing is unknown, although results are relatively insensitive to the details of the methodology.

Statistical significance was assessed by calculating the probability that the true spectrum exceeds the background by applying the bootstrap technique (e.g., Wilks 1995). This was done by calculating the means of 10 000 randomly selected (with replacement) sets of the power spectra of the windowed time–longitude segments that were used to find the original spectra. The location of the background value in this sampling distribution of the mean determines the significance level above the background. For example, if 95% of the distribution of means exceeded the background, then the spectrum is significant on the 95%. This significance test was applied to each point in the spectrum. Contours of significance level nearly parallel level contours of the normalized spectrum. These contours are not always parallel because the set of segments are not perfectly Gaussian.

REFERENCES

Carlson, T. N., 1969: Some remarks on African disturbances and their progress over the tropical Atlantic. *Mon. Wea. Rev.,* **97,** 716–726.

Chang, C.-P., and T. M. Piwowar, 1974: Effect of a CISK parameterization on tropical wave growth. *J. Atmos. Sci.,* **31,** 1256–1261.

Dickinson, M., and J. Molinari, 2002: Mixed Rossby–gravity waves and western Pacific tropical cyclogenesis. Part I: Synoptic evolution. *J. Atmos. Sci.,* **59,** 2183–2196.

Dunkerton, T. J., and F. X. Crum, 1995: Eastward propagating 2- to 15-day equatorial convection and its relation to the tropical intraseasonal oscillation. *J. Geophys. Res.,* **100,** 25 781–25 790.

Gu, G., and C. Zhang, 2001: A spectrum analysis of synoptic-scale disturbances in the ITCZ. *J. Climate,* **14,** 2725–2739.

Hayashi, Y., 1982: Space–time spectral analysis and its application to atmospheric waves. *J. Meteor. Soc. Japan,* **60,** 156–171.

Hendon, H. H., and B. Liebmann, 1991: The structure and annual variation of antisymmetric fluctuations of tropical convection and their association with Rossby–gravity waves. *J. Atmos. Sci.,* **48,** 2127–2140.

—— and M. L. Salby, 1994: The life cycle of the Madden–Julian oscillation. *J. Atmos. Sci.,* **51,** 2225–2237.

Hess, P. G., D. S. Battisti, and P. J. Rasch, 1993: Maintenance of the intertropical convergence zones and the large-scale tropical circulation on a water-covered earth. *J. Atmos. Sci.,* **50,** 691–713.

Kemball-Cook, S., and B. Wang, 2001: Equatorial waves and air–sea interaction in the boreal summer intraseasonal oscillation. *J. Climate,* **14,** 2923–2942.

Kleeman, R., 1989: A modeling study of the effect of the Andes on the summertime circulation of tropical South America. *J. Atmos. Sci.,* **46,** 3344–3362.

Kuo, H. L., 1975: Instability theory of large-scale disturbances in the tropics. *J. Atmos. Sci.,* **32,** 2229–2245.

Liebmann, B., and H. H. Hendon, 1990: Synoptic-scale disturbances near the equator. *J. Atmos. Sci.,* **47,** 1463–1479.

——, and C. A. Smith, 1996: Description of a complete (interpolated) outgoing longwave radiation dataset. *Bull. Amer. Meteor. Soc.,* **77,** 1275–1277.

Lindzen, R. S., 1967: Planetary waves on beta planes. *Mon. Wea. Rev.,* **95,** 441–451.

——, 1974: Wave-CISK in the Tropics. *J. Atmos. Sci.,* **31,** 156–179.

Madden, R. A., and P. R. Julian, 1994: Observations of the 40–50-day tropical oscillation—A review. *Mon. Wea. Rev.,* **122,** 814–837.

Matsuno, T., 1966: Quasi-geostrophic motions in the equatorial area. *J. Meteor. Soc. Japan,* **44,** 25–43.

Pires, P., J.-L. Redelsperger, and J.-P. Lafore, 1997: Equatorial atmospheric waves and their association to convection. *Mon. Wea. Rev.,* **125,** 1167–1184.

Randel, D. L., T. H. Vonder Haar, M. A. Ringerud, G. L. Stephens, T. J. Greenwald, and C. L. Combs, 1996: A new global water vapor dataset. *Bull. Amer. Meteor. Soc.,* **77,** 1233–1246.

Roundy, P. E., and W. M. Frank, 2004a: Effects of low-frequency wave interactions on intraseasonal oscillations. *J. Atmos. Sci.,* in press.

——, and ——, 2004b: Applications of a multiple linear regression model to the analysis of relationships between eastward- and westward-moving intraseasonal modes. *J. Atmos. Sci.,* in press.

Straub, K. H., and G. N. Kiladis, 2002: Observations of a convectively coupled Kelvin wave in the eastern Pacific ITCZ. *J. Atmos. Sci.,* **59,** 30–53.

——, and ——, 2003a: Extratropical forcing of convectively coupled Kelvin waves during austral winter. *J. Atmos. Sci.,* **60,** 526–543.

——, and ——, 2003b: Interactions between the boreal summer intraseasonal oscillation and higher-frequency tropical wave activity. *Mon. Wea. Rev.,* **131,** 945–960.

——, and ——, 2003c: The observed structure of convectively coupled Kelvin waves: Comparison with simple models of coupled wave instability. *J. Atmos. Sci.,* **60,** 1655–1668.

Takayabu, Y. N., 1994: Large-scale cloud disturbances associated with equatorial waves. Part I: Spectral features of the cloud disturbances. *J. Meteor. Soc. Japan,* **72,** 433–448.

——, and T. Nitta, 1993: 3–5 day disturbances coupled with convection over the tropical Pacific Ocean. *J. Meteor. Soc. Japan,* **71,** 221–245.

Wheeler, M., and G. N. Kiladis, 1999: Convectively coupled equatorial waves: Analysis of clouds and temperature in the wavenumber–frequency domain. *J. Atmos. Sci.,* **56,** 374–399.

——, ——, and P. J. Webster, 2000: Large-scale dynamical fields associated with convectively coupled equatorial waves. *J. Atmos. Sci.,* **57,** 613–640.

Wilks, D. S., 1995: *Statistical Methods in the Atmospheric Sciences: An Introduction.* International Geophysics Series, Vol. 59, Academic Press, 467 pp.

Yanai, M., and M. Murakami, 1970: Spectrum analysis of symmetric and antisymmetric equatorial waves. *J. Meteor. Soc. Japan,* **48,** 186–197.

Zhang, C., and P. J. Webster, 1989: Effects of zonal flows on equatorially trapped waves. *J. Atmos. Sci.,* **46,** 3632–3652.

Zhang, M., and M. A. Geller, 1994: Selective excitation of tropical atmospheric waves in wave-CISK: The effect of vertical wind shear. *J. Atmos. Sci.,* **51,** 353–368.